Welding in the World (2025) 69:3031–3052
https://doi.org/10.1007/s40194-025-02023-4

RESEARCH PAPER

Impact of sandwich joint on mechanical and ballistic performance of high-hardness armor steels

Ceren Çelik[1] · **Uğur Gürol**[2,3]

Received: 6 December 2024 / Accepted: 17 March 2025 / Published online: 28 March 2025
© The Author(s) 2025

Abstract

This study investigates the mechanical and ballistic performance of welded armor steel joints using two distinct filler materials, focusing on fully austenitic and sandwich joint configurations. Robotic gas metal arc welding (GMAW) was utilized to achieve precise and consistent welding parameters. The analysis thoroughly examined microstructure, hardness, tensile strength, Charpy impact toughness, and ballistic resistance. The fully austenitic joint offered excellent ductility and energy absorption but lacked the hardness to withstand ballistic impacts, resulting in complete penetration in the weld region. Conversely, the sandwich design, combining the exceptional toughness of the ASS layer with the superior hardness of the hard-faced interlayer, achieved excellent ballistic performance by resulting in only partial penetration (11 mm/15 mm of thickness). However, sandwich design led to a reduction in yield strength (41%), tensile strength (27%), elongation (62%), and toughness (48%) compared to the austenitic joint. It is also important to point out that in both designs, the heat-affected zone (HAZ) maintained hardness levels that were compliant with military standards (lower than 15.9 mm), ensuring structural reliability under impact conditions. Ballistic tests also confirmed that HAZ regions in both designs provided ballistic protection with a maximum penetration of 6.8 mm/15 mm. These findings underscore the balance between hardness and ductility in welded armor steels, offering critical insights for refining welding designs in defence applications. The study concludes that the sandwich design provides a robust solution for applications demanding high ballistic resistance, with potential implications for the defence industry in establishing new standards for welded armor steel joints.

Keywords Armor steel · Robotic gas metal arc welding · Sandwich joints · Ballistic resistance · Microstructural characterization · Mechanical properties

1 Introduction

Armor steels play a pivotal role in the defence industry, particularly in fabricating armored tanks, armored personnel carrier, military helmets, protective shields, and warships. These steels are specially designed to offer high hardness, strength, and toughness, enabling them to withstand and dissipate the kinetic energy from ballistic impacts [1, 2]. Their application is not limited to military vehicles; they are also extensively used in civilian sectors for security purposes, including armored vehicles for the safe transport of personnel and valuables, protective cabins, bulletproof doors, bank vaults, and safe rooms. The inherent strength and toughness of these materials make them ideal for this kind of application. The production of armor steels typically involves quenching and tempering processes, which optimize their mechanical properties to ensure superior performance in high-stress environments [3, 4]. However, the complex geometries of armored vehicles necessitate joining multiple sections, as monolithic production of significant components is not feasible. This requirement introduces the critical need for effective welding processes [5].

Recommended for publication by Commission II - Arc Welding and Filler Metals.

✉ Uğur Gürol
ugur.gurol@yahoo.com

[1] Faculty of Engineering, Department of Mechanical Engineering, Istanbul Gedik University, 34876 Istanbul, Turkey

[2] Faculty of Engineering, Department of Metallurgical and Materials Engineering, Istanbul Gedik University, 34876 Istanbul, Turkey

[3] Istanbul Vesuvius Refrakter A.Ş, FOSECO Foundry Division, 41420 Kocaeli, Turkey

Welding armor steels, however, presents significant challenges due to their high carbon equivalent (CE), which increases susceptibility to hydrogen-induced cracking (HIC) and other issues, significantly hardening and softening in the heat-affected zone (HAZ) [6–8]. These challenges are exacerbated by the need to maintain the mechanical and ballistic integrity of the joints, making the development of optimized welding processes a critical area of research. The armor steels can be welded using several techniques, including shielded metal arc welding (SMAW), flux cored arc welding (FCAW), gas metal arc welding (GMAW), and gas tungsten arc welding (GTAW) [9]. The choice of welding method depends on various factors such as the steel's chemical composition, the thickness of the armor plates, and the complexity of the product [10]. Among these techniques, GMAW stands out due to its higher deposition rates and lower heat input, which makes it particularly suitable for welding armor steels. Therefore, researchers recently focused on GMAW to improve the weldability of armor steels, although some also addressed FCAW, which uses a flux-filled tubular wire instead of a solid wire [11–13].

In general, the design approach favors the use of welding filler materials with a higher yield strength than the base material (over-matching), to enhance the welded region's resistance to structural loads. However, this approach is not always feasible for armor steels due to their higher susceptibility to hydrogen-induced cracking. Therefore, matching or overmatching wires should be avoided to achieve crack-free joints while enhancing toughness and ductility [14]. HIC in armor steel welds can be managed using three methods: temperature control, isothermal transformation, and the use of austenitic stainless steel (ASS) welding consumables. The temperature control method includes maintaining the weld at high temperatures to accelerate hydrogen diffusion, while the isothermal transformation method regulates the cooling rate to prevent the formation of martensitic structures in the heat-affected zone (HAZ). It is not always possible to employ preheat temperature greater than 150 °C in industrial conditions, therefore the temperature control method is severely limited and the isothermal transformation method cannot be used [5]. In this context, the most effective approach is using ASS welding consumables due to their superior hydrogen solubility in the austenitic phase, which aids in mitigating hydrogen-induced cracking (HIC) [15]. Particularly as plate thickness increases, the requirement for preheating becomes inevitable, making the use of ASS consumables more industrially viable for achieving defect-free welds under less stringent conditions. Magudeeswaran et al. [5] examined HIC in quenched and tempered (Q&T) steel weldments using shielded metal arc welding (SMAW) and flux-cored arc welding (FCAW) with ASS and low hydrogen ferritic (LHF) consumables. Their findings indicated that FCAW with ASS consumables provided superior resistance to HIC, attributed to lower diffusible hydrogen content and favorable microstructural characteristics, surpassing the performance of LHF and SMAW techniques. Similarly, Kumar et al. [16] investigated the impact of various welding consumables on the mechanical properties of ultra-high hard armor steel joints welded using SMAW. They observed that joints welded with LHF electrodes exhibited the highest tensile strength (962 MPa), while those welded with ASS electrodes demonstrated significantly better impact toughness (72 J). Additionally, Saxena et al. [17] reported that in SMAW-welded Armox 500 T joints, LHF consumables achieved higher joint efficiency (41.7%) compared to ASS (30.6%), though ASS welds provided 20% greater impact toughness than the base metal, making them preferable for applications where impact resistance is critical. Furthermore, in another study by Kumar et al. [18] it was noted that the use of ASS electrodes in SMAW-welded armor joints resulted in superior ballistic resistance, evidenced by a shallow penetration depth (9 mm) and low area density (70 kg/m^2). Conversely, while LHF electrodes offered higher tensile strength, they led to greater penetration depths, suggesting inferior ballistic protection.

Among the most critical regions in welded armor steel joints is the heat-affected zone (HAZ), which often dictates the overall performance of the joint in ballistic applications [19]. Because the HAZ is prone to softening due to the thermal cycles experienced during welding, leading to a reduction in hardness and toughness in this region [20]. This softening effect can significantly impair the ballistic performance of the welded joints, as these areas are more susceptible to failure under high-impact conditions. As an example, Savic and Cabrilo [21] compared the ballistic performance of Protac 500 armor steel welded with heat inputs of 1.29 kJ/mm and 1.55 kJ/mm. They found that the lower heat input of 1.29 kJ/mm resulted in superior ballistic resistance and better hardness retention in the HAZ. In contrast, the 1.55 kJ/mm weldment had a wider softened HAZ and reduced ballistic performance. Similarly, Coban et al. [22] studied the impact of heat input on the microstructure and hardness of fillet welded Protection 600 armor steel. They found that higher heat input resulted in a wider heat-affected zone (HAZ) and significant softening, with the hardness dropping below military standards at 1.2 kJ/mm. Therefore, continuous efforts are needed to improve the mechanical properties of these critical regions to ensure they can meet the stringent demands of ballistic environments.

On the other hand, it has been reported that the ballistic performance of armor steel plates was initially enhanced in the late 1800s by layering or hardening their surfaces with materials possessing different properties. For instance, Choo et al. [23] investigated the ballistic impact behavior of multilayered armor plates processed with various hard-facing combinations. They reported that multilayered armor plates, consisting of a hard high-chromium layer combined with a softer stainless steel layer, exhibited increased ballistic performance. In another recent study, Babu et al. [24] studied the effect of plasma transferred arc (PTA) hard facing on the ballistic performance of armor steel weldments. They found that welds with a tungsten carbide hard-faced interlayer significantly improved ballistic resistance, preventing projectile penetration, while welds without the interlayer failed under impact. The addition of the hard-faced layer increased the ballistic limit by 5.25 times compared to welds without it, demonstrating enhanced protection equivalent to the base metal. Similarly, Reddy et al. [25] aimed to enhance the ballistic resistance of austenitic welds on 6-mm plates using hard-facing. They found that fully hard-faced welds, despite being harder (at least 2.5 times) compared to fully austenitic welds, shattered on impact, compromising their integrity. Their findings indicated that while austenitic welds offered some ballistic protection, hard facing alone was ineffective and led to failure due to cracking.

On the other hand, in recent years, a new method referred to as "sandwich welding" has attracted considerable interest [26]. Only a few amounts of researchers focused on this approach, which involves utilizing two or even three different welding wires in a single weld joint and combining their properties to enhance the ballistic performance of armor plates. For instance, Balakrishnan et al. [27] studied the effect of hard-faced interlayer thickness and low hydrogen ferritic (LHF) capping on the ballistic performance of shielded metal arc welded armor steel joints.nn They found that increasing the hard-faced layer thickness enhanced ballistic resistance, reducing penetration depth to 1.5 mm. The LHF capping further improved toughness and minimized cracking, bolstering the join's overall integrity under ballistic impact. Balakrishnan et al. [28], in their other study, investigated the effect of capping front layers on the ballistic performance of quenched and tempered (Q&T) steel joints. Their findings indicated that the LHF capping front layer provided superior resistance against penetration by a 7.62-mm armor-piercing projectile compared to the SS layer. This enhanced performance was attributed to the gradual increase in hardness resulting from a bimodal acicular ferrite/bainite microstructure. Although earlier limited studies have indicated that ballistic performance can be improved by adding a hard-faced deposit layer between and/or on top of the softer austenitic stainless steel (ASS) layers, the main design priorities for most armor steel plates should concentrate on achieving high-yield strength, ultimate tensile strength, elongation at ambient temperature, and transverse Charpy impact energy at – 40 °C [29]**.** Because, these parameters are crucial for ensuring that armor steels can withstand the demanding conditions they are subjected to, including maintaining structural integrity and impact resistance under extremely cold temperatures. Therefore, this study aims to address this gap for sandwich welding design by comprehensively evaluating microstructural, mechanical, and ballistic properties, including optical microscopy, electron backscatter diffraction analysis (EBSD), hardness, tensile strength, Charpy impact toughness, and ballistic resistance, all within a single investigation. The findings presented here are expected to have practical implications for armored vehicle manufacturing, where both mechanical strength and ballistic resistance are critical. Moreover, the insights obtained from this research could guide future investigations focused on developing more advanced welding techniques and materials tailored for the defence sector.

2 Experimental studies

In this study, 15 mm thick high-hardness ballistic armor steel plates from the Protection 500 series, manufactured by Miilux-OY, were used. Before welding, the plates were prepared according to the EN ISO 9692–1 standard and were machined to have a single-sided bevel angle of 30°. The bevelled edges of the plates were thoroughly cleaned to remove any oil, dirt, or contaminants. A liquid penetrant inspection was conducted to detect any potential cracks or defects in the weld preparation area. A 2 mm chamfer was applied to the welding edges, creating a 2 mm root gap. Additional steel pieces were tack-welded to the start and end points of the plates to facilitate the welding process. To achieve full penetration from a single side, ceramic backing was employed, as shown in Fig. 1.

Table 1 illustrates the chemical compositions of the base metal (armor steel) and the filler materials (austenitic and hard facing). The base metal, armor steel, consists of 0.21% C, 1.02% Mn, 0.49% Si, 0.62% Cr, 0.42% Ni, and 0.29%

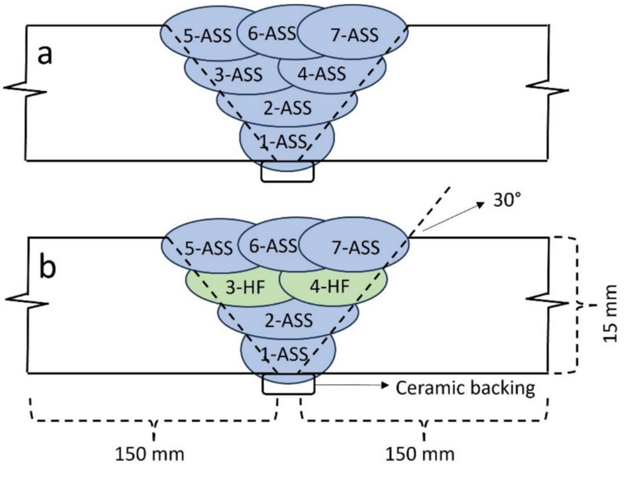

Fig. 1 Schematic illustration of joint design and sequence of welding: **a** fully austenitic and **b** sandwich (hard-faced) joint

Table 1 Chemical composition of the base metal and filler materials used (wt.%)

Materials	C	Mn	Si	Cr	Ni	Mo
Armor steel (base metal, BM)	0.21	1.02	0.49	0.62	0.42	0.29
Austenitic stainless steel wire (ASS)	0.06	5.85	0.61	17.82	7.92	0.02
Hardfacing wire (Hardcor 600G)	0.33	0.60	0.54	8.53	0.18	0.00

Mo. These elements provide the steel with high strength and hardness, which is essential for its application in ballistic protection. The relatively low chromium and nickel content contributes to the overall toughness and weldability of the steel. The austenitic filler material, SG307, shows significantly higher levels of Mn (5.85%), Cr (17.82%), and Ni (7.92%) compared to the base metal. This ASS wire was selected for both joints because it effectively inhibits the risk of delayed cracking in the Q&T steel weldments, as previously discussed. The high chromium content in the austenitic filler promotes the formation of δ-ferrite during the welding process, which is beneficial for preventing solidification cracking. The substantial nickel content stabilizes the austenitic phase, enhancing the toughness and ductility of the weld metal. The hard-facing filler material (GeKa Hardcor 600G), characterized by 0.33% C, 0.60% Mn, 0.54% Si, 8.53% Cr, and 0.18% Ni, was employed in the sandwich design to enhance the weld's ballistic resistance. The high chromium content contributes to the formation of carbides and martensite, significantly increasing the hardness and wear resistance of the weld metal. This hard-facing layer, introduced between the root and cap passes of the sandwich weld, is described in Fig. 1b.

Table 2 presents the certified mechanical properties of the base metal (armor steel) and the filler materials (welding wire and hardfacing wire) used in this study. The armor steel demonstrates a high yield strength of 1324 MPa and a tensile strength of 1689 MPa. These values reflect the material's capability to endure significant stress and strain before failure, which is essential for ballistic protection applications. The Charpy impact energy of 30 J at − 40 °C indicates the armor steel's ability to absorb energy during impact, ensuring its toughness under extreme conditions. The ASS welding wire used exhibits a minimum yield strength of 370 MPa and a tensile strength ranging from 580 to 750 MPa. Although these values are lower than those of the base metal (undermatching), they are sufficient to maintain the integrity of the weld joint under typical service conditions. The Charpy impact energy of the welding wire is a minimum of 63 J at + 20 °C), highlighting its superior toughness and energy absorption capability at room temperature. This characteristic is vital for the welded regions, as it helps to dissipate energy and prevent fracture under sudden impacts or explosive forces. This is beneficial in certain scenarios, such as in armored vehicles, where the weld zones are often placed in concealed locations, providing an additional layer of protection. The hard-facing wire stands out with its exceptional hardness, rated at 600 HB. This high hardness level is achieved by forming martensite and metal carbides (MC), making the hard-facing layer highly resistant to wear and impact. The primary purpose of incorporating the hard-facing wire in the sandwich design is to create an intermediate layer that can endure high-stress impacts and enhance the overall ballistic performance of the welded joint.

The welding process was performed using a robotic gas metal arc welding (GMAW) technique to ensure high deposition rates and stable welding conditions (Fig. 2a). Specifically, the GMAW process employed a GeKa-Mac WB 500 L GMAW welding machine equipped with a water-cooled torch, which was mounted on a 6-axis OTC Daihen FD-V8L industrial robot (Fig. 2). The use of robotic GMAW allows for precise control over welding parameters, ensuring consistent heat input and minimizing the variability that can lead to defects in the weld. This precision not only reduces the likelihood of human error but also enables higher welding speeds, improving overall efficiency. Furthermore, the repeatability and accuracy of robotic welding systems ensure that each weld meets stringent quality standards, which is particularly important in the production of armor steels where the integrity of the joint is critical. In addition, the weave bead technique was applied to all passes except for the root passes in both joints, and preheating of the armor steel plates was carried out based on the carbon equivalent of the material. Using a propane torch, the plates were uniformly

Table 2 Certified mechanical properties of base metal and filler materials used

	Yield strength (MPa)	Tensile strength (MPa)	Charpy impact energy (J)	Hardness (HB)
Armor steel	1324	1689	30 (ISO-V/−40 °C)	-
Welding wire	Min. 370	580–750	Min.63 (ISO-V/ + 20 °C)	-
Hardfacing wire	-	-	-	600

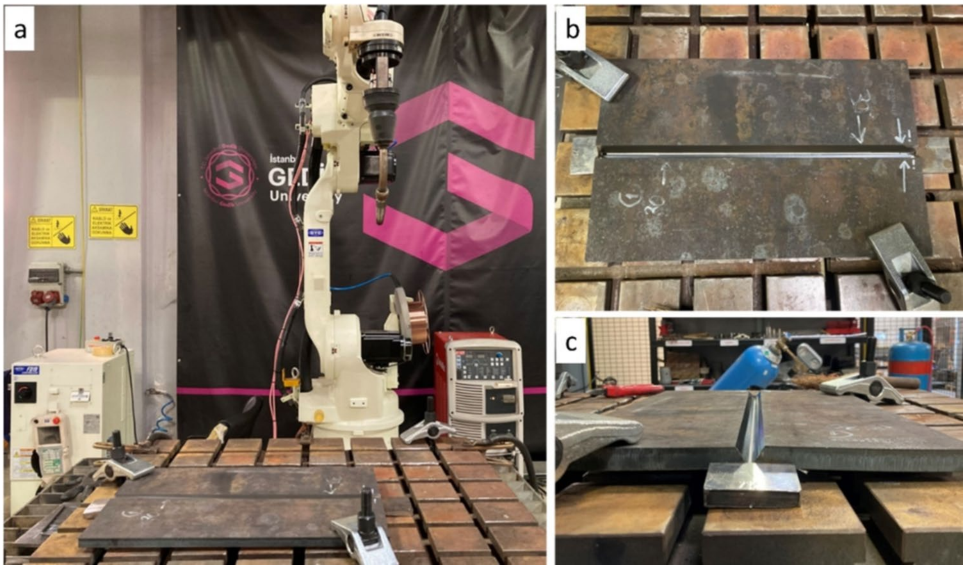

Fig. 2 **a** Robotic GMAW welding unit, **b** top, and **c** side view of welding plates

Table 3 The welding parameters used during the fabrication of fully austenitic and sandwich joints

Parameters	Units	Austenitic wire	Hard-facing wire
Wire diameter	mm	1.2	1.2
Current	A	195–205	185–210
Voltage	V	17–20	21–22
Welding speed	cm/min	25–29	26
Contact tip to workpiece distance	mm	13	13
Shielded gas	-	$ArCO_{2,5}$	CO_2–%100
Gas flow rate	l/min	18	18
Welding position	-	PA	PA
Heat input	kJ/mm	0.80–0.87	0.90–1.10

heated to a preheating temperature of 120 ± 10 °C. This preheating step was crucial to reduce the risk of hydrogen-induced cracking and to ensure better fusion of the weld metal with the base metal. The welding was conducted in multiple passes, with careful attention paid to the interpass temperature, which was maintained below 150 ± 15 °C to avoid excessive heat accumulation. The temperature was measured following the ISO 13916:2017 standard, using a Fluke 62 Mini Infrared thermometer, with readings taken 60 mm from the weld groove.

The parameters used during the fabrication of fully austenitic and sandwich joints are outlined in Table 3. The fully austenitic joint utilized an arc current of 195–205 A, a voltage of 17–20 V, and a welding speed of 25–29 cm/min, with $ArCO_{2,5}$ as the shielding gas. In comparison, the sandwich joint was welded with an arc current of 185–210 A, a voltage of 21–22 V, and a welding speed of 26 cm/min, using 100% CO2 as the shielding gas. Both processes maintained a gas flow rate of 18 l/min, and the heat input ranged from 0.80 to 0.87 kJ/mm for the austenitic joint to 0.90–1.10 kJ/mm for the sandwich joint. These parameters, along with the controlled preheating and inter-pass temperature, ensured optimal welding conditions and high-quality joint fabrication.

After welding, the plates were air-cooled and subjected to non-destructive testing to detect any discontinuities. Visual inspection was conducted according to TS EN ISO 17637, followed by liquid penetrant testing as per TS EN ISO 3452–1 and radiographic testing in compliance with TS EN ISO 17636–1, with evaluations based on the relevant standards. Metallographic examination involved macro and microstructural analyses, using standard preparation and etching techniques. A Leica DMI8 M microscope was used for detailed microstructural examination, and SEM analysis was performed on fracture surfaces to investigate failure mechanisms. The chemical composition was verified using OES and XRF spectrometers, and δ-ferrite content in austenitic welds was measured with a Fischer Feritscope FMP30.

Vickers hardness testing was performed on the weld metal, HAZ, and base metal at 0.5 mm intervals using an Emcotest Durascan microhardness tester to detect hardness variations and HAZ softening. Tensile tests were conducted according to EN ISO 4136 and EN ISO 6892–1, while Charpy impact tests were performed at − 40 °C following EN ISO 148–1 and EN ISO 9016, to evaluate toughness under low-temperature conditions. Finally, ballistic testing was conducted with 7.62 × 51 mm P80 NATO AP ammunition according to EN 1522 FB7 standards (weight of bullet: 9.8 ± 0.1 g, shooting distance: 10 ± 0.5 m and bullet velocity: 820 ± 10 m/s), followed by post-test metallographic analysis to assess the impact on weld integrity.

3 Results and discussion

The initial assessment of the welded joints included visual and penetrant testing, followed by X-ray radiographic examination, to verify the welds' integrity and quality. The results from visual testing (VT) and penetrant testing (PT) for both the fully austenitic and sandwich designs, as illustrated in Fig. 3, confirmed that no surface defects were present. The VT images (Fig. 2a and c) and PT images (Fig. 2b and d) were evaluated according to the EN ISO 5817 standard, achieving a quality level B, indicating a high-quality surface free from detectable flaws.

Subsequently, X-ray testing, depicted in Fig. 4, provided a detailed analysis of the internal structure of the welds. The radiographic images (Fig. 4a and b) corroborated the external test results, revealing no internal defects such as cracks, porosities, or inclusions within the weld metal or the heat-affected zone. These consistent findings obtained from each non-destructive testing confirm that the welding techniques were carefully controlled and precisely executed, resulting in high-quality welds that are well-suited for high-strength armor steel applications.

The macrostructure of both the fully austenitic weld (Fig. 5a) and the sandwich weld (Fig. 6a) reveals a uniform weld profile with smooth, distinct weld passes, indicating that the welding parameters were well-managed. However, the sandwich weld design (Fig. 6a) also features a clearly defined hard-facing layer in addition to the standard weld passes. Previous studies [30] reported that placing a

Fig. 3 Visual and penetrant testing results for weld joints: VT (**a**, **c**) and PT (**b**, **d**) for austenitic and sandwich desings, respectively

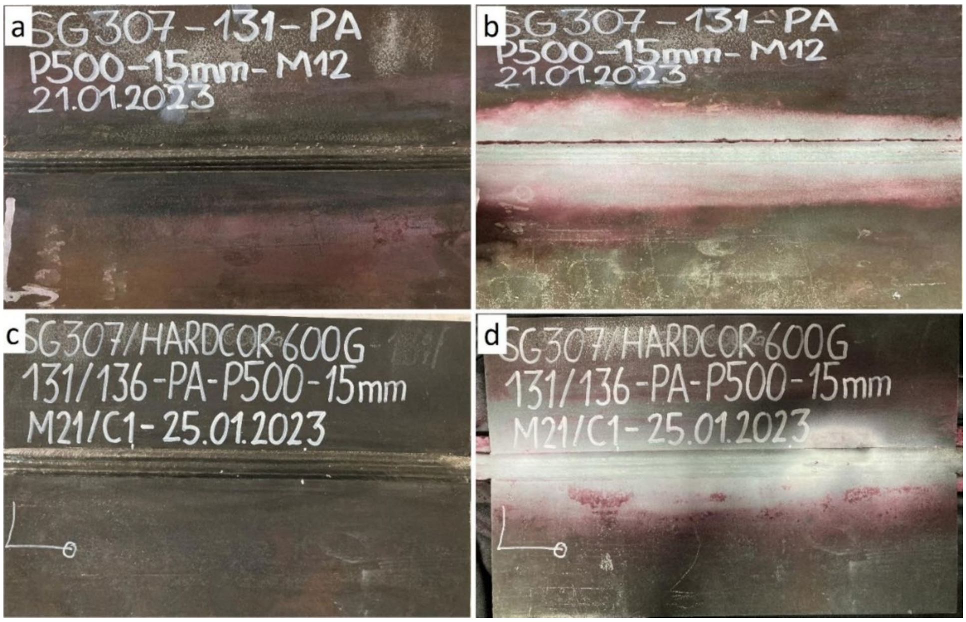

Fig. 4 X-ray testing results: **a** sandwich and **b** austenitic design

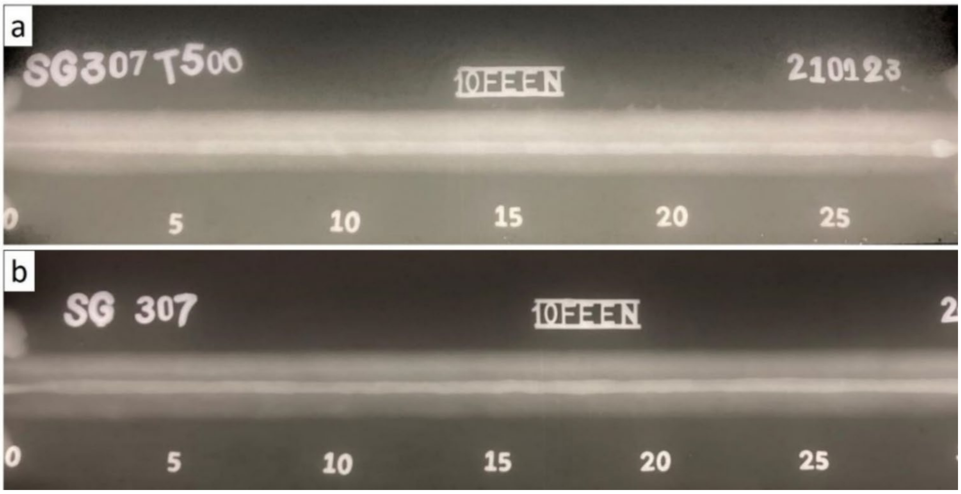

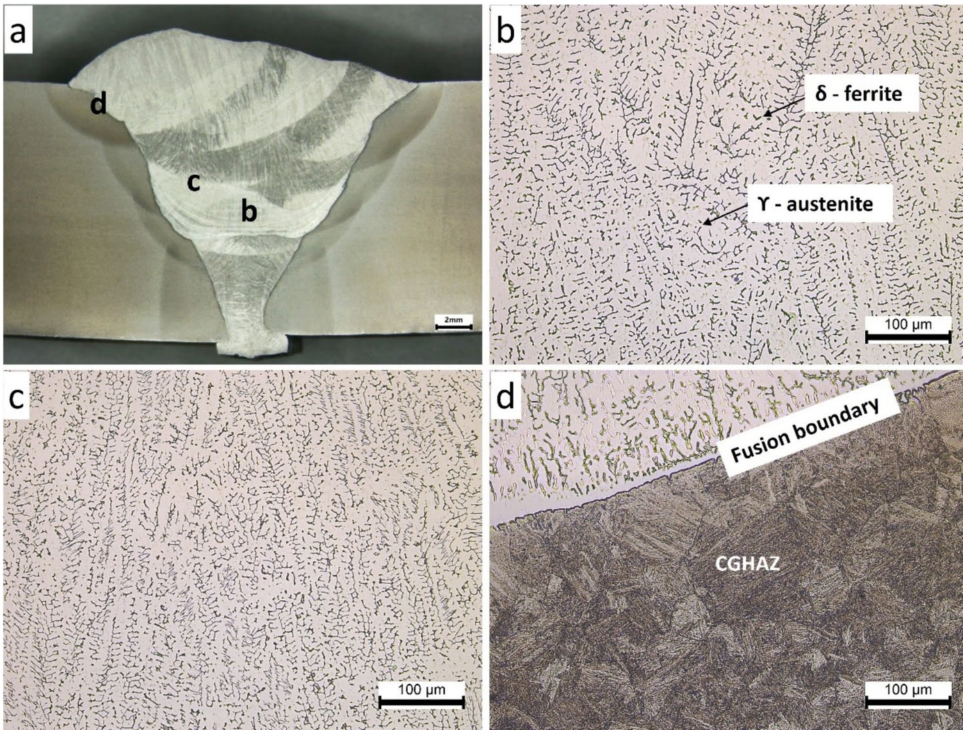

Fig. 5 **a** Macrostructure of austenitic design, microstructure of the weld metal (**b**, **c**), and heat-affected zone (**d**)

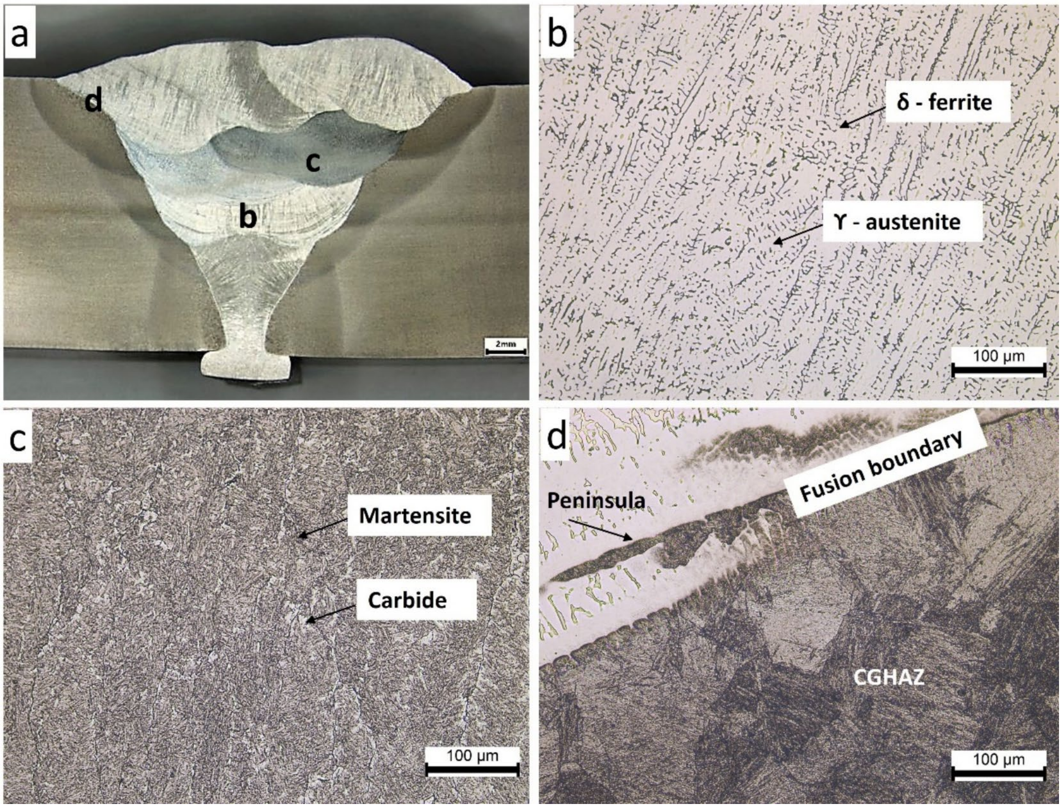

Fig. 6 **a** Macrostructure of sandwich design, microstructure of the weld metal (**b**, **c**), and heat-affected zone (**d**)

hardfacing alloy weld between ASS welds can lead to cracks at the interface, primarily due to the brittle nature of the hardfacing alloy. However, in our study, welding parameters, mainly focusing on preheating temperatures, were optimized to address this issue and confirmed that it meet the minumum quality requirements of ISO 5818-B.

In the weld metal region of the fully austenitic design (Fig. 5b) and sandwich design (Fig. 6b), the microstructure predominantly consists of δ-ferrite and γ-austenite phases. This duplex structure, supported by the high chromium content in the SG307 filler material, offers a balanced combination of toughness and ductility, while also helping to prevent solidification cracking. When examining the central weld metal region, the fully austenitic design (Fig. 5c) maintains a consistent microstructure of δ-ferrite and γ-austenite, ensuring uniform mechanical properties across the weld. In contrast, the sandwich design (Fig. 5c) exhibits a more complex microstructure, characterized by a mix of martensite and carbides. The introduction of the hard-facing layer leads to the formation of these phases, which enhance hardness but may reduce the overall toughness compared to the fully austenitic weld.

The fusion boundary and coarse-grain heat-affected zone (CGHAZ) of austenitic and sandwich designs were presented in Figs. 5d and 6d, respectively. In both designs, the fusion boundary shows a smooth transition with a combination of δ-ferrite and γ-austenite near the weld metal. However, the coarse-grained HAZ that experienced the peak temperature ($\gg$ Ac3 temperature) are visible for both designs, and they are characterized by the presence of coarse primary austenite grains and coarse martensite structure as reported in previous studies [6]. The CGHAZ in each design contains a significant amount of martensite, resulting from the high carbon content and rapid cooling rates. On the other hand, the unmixed zone (UZ) at the interface of the sandwich design, resulting from the partial mixing of molten metal between the base metal and the ASS filler, can be seen in Fig. 6d. Macroscopic solute segregation, forming features like peninsulas, islands, and beaches, is commonly observed across dissimilar weldments [31]. The peninsula-type segregation, having similar compositions to the base metal and seen parallel to the fusion boundary in Fig. 6d, indicates that these formations originate from the melted but unmixed base metal, independent of the filler composition [32].

Figure 7 presents the ferrite content measurements across various regions of the austenitic and sandwich weld designs, as determined using a Fischer Feritscope FMP30. The results indicate regional variations in ferrite content, influenced by dilution effects and the type of welding wire employed. In the root areas, both designs exhibit lower ferrite content in the central regions compared to the edges, likely due to reduced base metal dilution in the central sections. In the face regions, the austenitic design shows higher ferrite content compared to the sandwich design. This difference can be attributed to the presence of the hard-facing layer in the sandwich design, which leads to carbon and chromium diffusion, subsequently reducing ferrite content in the final pass. Additionally, a significant increase in ferrite content is noted in the middle section of the sandwich design, which is likely due to the presence of magnetic martensitic phases. This variation underscores the complex interactions between different phases and the considerable influence of the hard-facing material on the overall composition of the weld.

Figure 8 showcases the microstructure and phase distribution across different regions of the sandwich weld joint, with a focus on the roles played by iron phases and chromium carbides. In the hard-faced layer (Fig. 8a, b), a predominantly martensitic structure is observed, enriched with chromium carbides such as $Cr_{23}C_6$ and Cr_7C_3. These carbides are critical for enhancing hardness, key factors for the joint's performance in ballistic applications. As we move to the HAZ between the base metal and the hard-faced layer (Fig. 8c, d), a mixed microstructure consisting of martensite and retained austenite is evident, with a slightly lower concentration of carbides. The transition zone between the hard-faced layer and the austenitic layer (Fig. 8e, f) reveals a sharp contrast in phase composition, with concentrated carbides near the interface, highlighting the challenges of achieving seamless material integration. In the HAZ between the austenitic layer and the base metal (Fig. 8g, h), a gradual transition

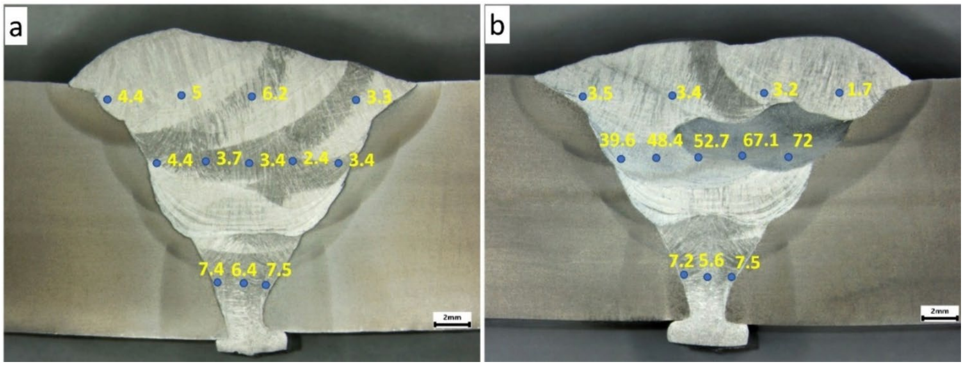

Fig. 7 Ferrite contents of **a** austenitic and **b** sandwich design

Fig. 8 Phase fraction of different region for sandwich joint; **a**, **b** hard-faced layer; **c**, **d** HAZ between base metal and hard-faced layer; **e**, **f** transition region between hard-faced layer and austenitic region; **g**, **h** HAZ between austenitic layer and base metal; and **i**, **j** austenitic layer

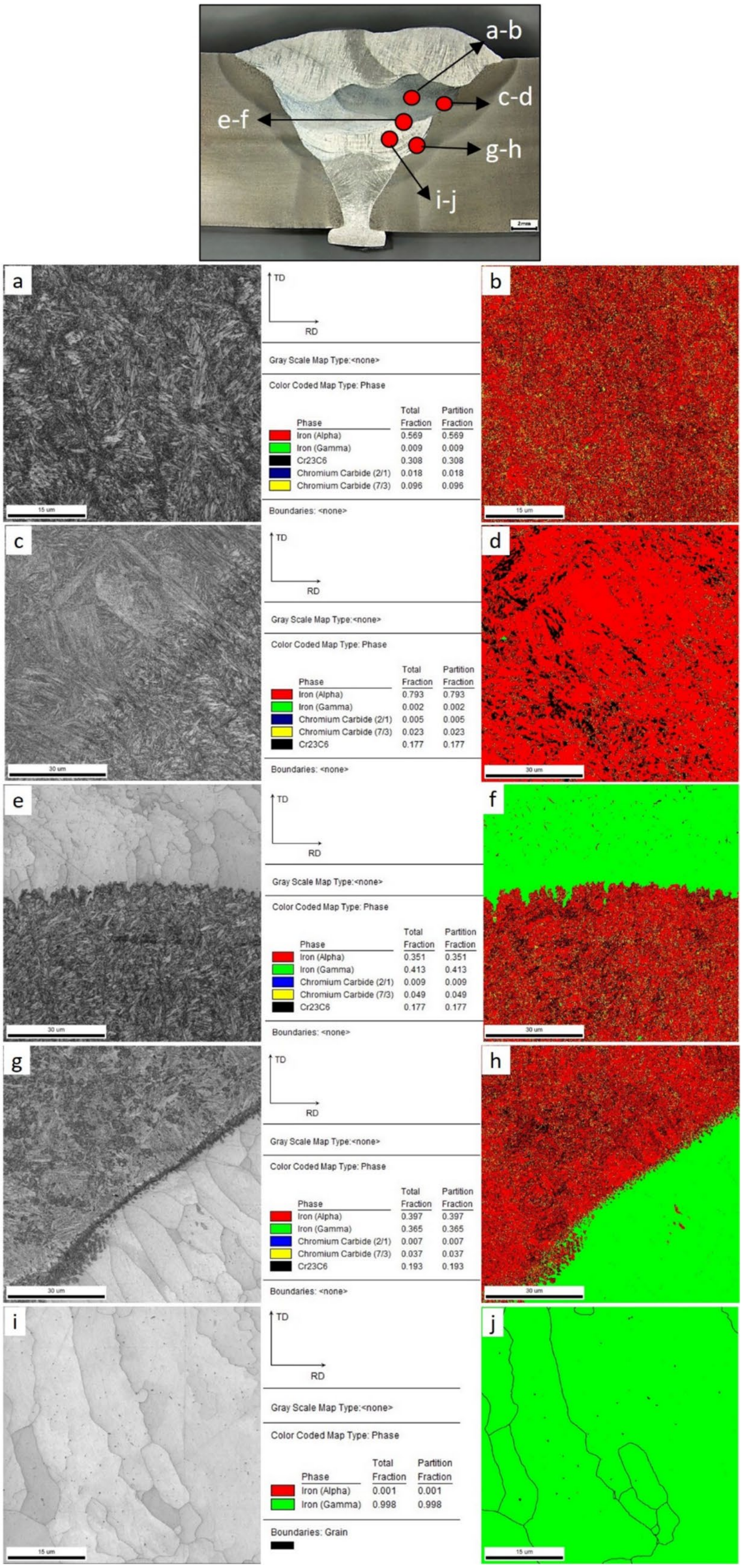

Gray Scale Map Type:<none>

Color Coded Map Type: Phase

	Phase	Total Fraction	Partition Fraction
🟥	Iron (Alpha)	0.569	0.569
🟩	Iron (Gamma)	0.009	0.009
⬛	Cr23C6	0.308	0.308
🟦	Chromium Carbide (2/1)	0.018	0.018
🟨	Chromium Carbide (7/3)	0.096	0.096

Boundaries: <none>

Gray Scale Map Type:<none>

Color Coded Map Type: Phase

	Phase	Total Fraction	Partition Fraction
🟥	Iron (Alpha)	0.793	0.793
🟩	Iron (Gamma)	0.002	0.002
🟦	Chromium Carbide (2/1)	0.005	0.005
🟨	Chromium Carbide (7/3)	0.023	0.023
⬛	Cr23C6	0.177	0.177

Boundaries: <none>

Gray Scale Map Type:<none>

Color Coded Map Type: Phase

	Phase	Total Fraction	Partition Fraction
🟥	Iron (Alpha)	0.351	0.351
🟩	Iron (Gamma)	0.413	0.413
🟦	Chromium Carbide (2/1)	0.009	0.009
🟨	Chromium Carbide (7/3)	0.049	0.049
⬛	Cr23C6	0.177	0.177

Boundaries: <none>

Gray Scale Map Type:<none>

Color Coded Map Type: Phase

	Phase	Total Fraction	Partition Fraction
🟥	Iron (Alpha)	0.397	0.397
🟩	Iron (Gamma)	0.365	0.365
🟦	Chromium Carbide (2/1)	0.007	0.007
🟨	Chromium Carbide (7/3)	0.037	0.037
⬛	Cr23C6	0.193	0.193

Boundaries: <none>

Gray Scale Map Type:<none>

Color Coded Map Type: Phase

	Phase	Total Fraction	Partition Fraction
🟥	Iron (Alpha)	0.001	0.001
🟩	Iron (Gamma)	0.998	0.998

Boundaries: Grain

from austenitic to martensitic phases is observed, with fewer carbides present, balancing the hardness with the necessary ductility. The austenitic layer (Fig. 8i, j) shows a uniform microstructure with minimal carbide content, ensuring the weld's overall toughness and fracture resistance. The distribution of carbides and phases across these regions underscores the complex thermal and mechanical interactions during welding, with the hard-faced layer providing enhanced surface hardness while the austenitic layer maintains ductility, crucial for the joint's performance under dynamic loading. This is consistent with findings in the literature regarding multi-layer welds used in high-stress applications.

Figure 9 presents inverse pole figure maps, offering a crystallographic orientation analysis across the same regions examined in Fig. 8. The hard-faced layer (Fig. 9b) exhibits a strong texture, indicative of the directional solidification that occurs with high cooling rates and the presence of martensitic phases. Understanding this crystallographic orientation is essential for assessing the mechanical anisotropy of the layer, which may affect the joint's response to stress. In the HAZ between the base metal and the hard-faced layer (Fig. 9c), a more random grain orientation is observed, reflecting the thermal and mechanical influences during welding. This randomization of grain orientation can be advantageous, as it may reduce the likelihood of crack propagation along specific crystallographic planes. The transition zone between the hard-faced layer and the austenitic layer (Fig. 9d) shows a mix of orientations, corresponding to the diverse phase composition in this area. The complexity of grain orientation in this region highlights the challenge of achieving a homogenous structure when integrating different materials. The HAZ between the austenitic layer and the base metal (Fig. 9e) exhibits a more uniform grain orientation, transitioning towards the typical equiaxed grains found in the austenitic layer (Fig. 9f). This uniformity in grain orientation is crucial for maintaining the mechanical properties of the austenitic weld metal, ensuring consistency throughout the joint.

Figure 10 provides a detailed analysis of the crystallographic texture across the sandwich design, with pole figures illustrating key regions. The colors in the pole figures represent different orientations, with red indicating high-intensity peaks that correspond to preferred crystallographic orientations, while blue and green areas denote lower-intensity regions with more random orientations. The hard-faced layer (Fig. 10a) shows a strong texture with high-intensity peaks reaching up to approximately 8 multiples of a random distribution (m.r.d.). This significant peak suggests a pronounced preferred orientation, likely resulting from the directional solidification of martensitic phases and chromium carbides during rapid cooling. This strong texture may contribute to anisotropic mechanical properties, where the material exhibits different strengths in different directions. The HAZ between the base metal and the hard-faced layer (Fig. 10b) shows a moderate texture with peaks around 5 m.r.d. The reduction in peak intensity compared to the hard-faced layer indicates a more randomized grain orientation, reflecting the thermal effects and phase transitions that occur during welding. The pole figure for the transition region between the hard-faced layer and the austenitic layer (Fig. 10c) shows a more diffused texture with peaks around 3 m.r.d. This lower intensity highlights the complex interaction between the hard-facing material and the austenitic filler, resulting in a mixed crystallographic orientation. The reduced peak intensity suggests that the material in this region has less pronounced directional properties, potentially leading to more isotropic mechanical behavior. The HAZ between the austenitic layer and the base metal (Fig. 10d) shows peaks of around 2 m.r.d., indicating a further decrease in preferred orientation. The more randomized grain structure here reflects the influence of the austenitic filler material, promoting the formation of equiaxed grains with a more uniform orientation. The pole figure for the austenitic layer shows the lowest peak intensity, around 1.5 m.r.d., indicating a near-random orientation. This lack of strong texture is typical of austenitic structures, which are characterized by equiaxed grain formations. This uniform grain orientation contributes to the isotropic nature of the austenitic weld metal, ensuring consistent mechanical properties regardless of the direction of applied stress.

Kernel average misorientation (KAM) maps presented in Fig. 11 further explore the strain distribution across the weld. The hard-faced layer (Fig. 11a) exhibits high misorientation values, corresponding to the significant internal stresses generated during the rapid solidification and phase transformation processes. Understanding these stress concentrations is crucial for identifying potential failure points in this layer under mechanical loads. In the HAZ (Fig. 11b–d), the misorientation decreases, indicating stress relaxation as the structure transitions away from the hard-faced layer. The austenitic layer (Fig. 11e) shows the lowest misorientation, reflecting its ability to accommodate deformation without significant internal stress buildup, a key factor in maintaining joint integrity under dynamic loading conditions.

Figure 12 presents the hardness testing results, showing the measurements taken across each layer, starting from the base metal, progressing through the HAZ, and into the weld metal for both the austenitic joint (Fig. 12a) and the sandwich joint (Fig. 12b). Neither joint displays a uniform hardness distribution; instead, there are notable variations as the hardness changes from the base metal to the weld region. These variations are influenced by the thermal cycles, dilution rate, and microstructural changes that occur during the welding process [33]. For instance, the hardness values for each layer or pass in the austenitic joint are as follows: 196 ± 9 HV in the fifth (face) pass, 204 ± 8 HV in the fourth,

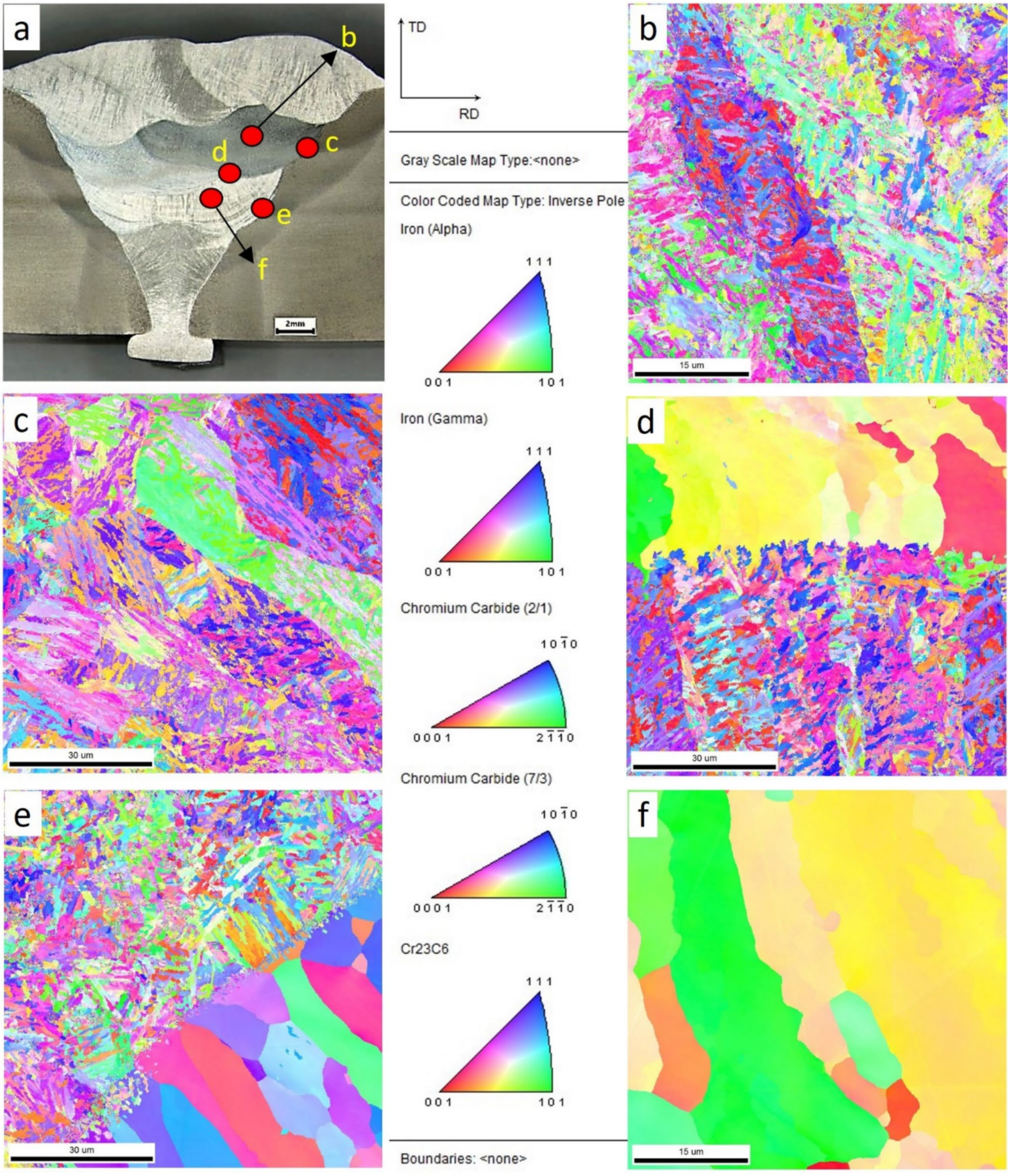

Fig. 9 Inverse pole figure maps; **a** showing the interested points, **b** hard-faced layer, **c** HAZ between base metal and hard-faced layer, **d** transition region between hard-faced layer and austenitic region, **e** HAZ between austenitic layer and base metal, and **f** austenitic layer

213 ± 9 HV in the third pass, 205 ± 15 HV in the second, and 225 ± 20 HV in the first (root) pass. This pattern generally shows an increase in hardness towards the weld pass, though there are fluctuations between the layers. These fluctuations can be attributed to the complex interactions between thermal effects and the formation of δ-ferrite and γ-austenite

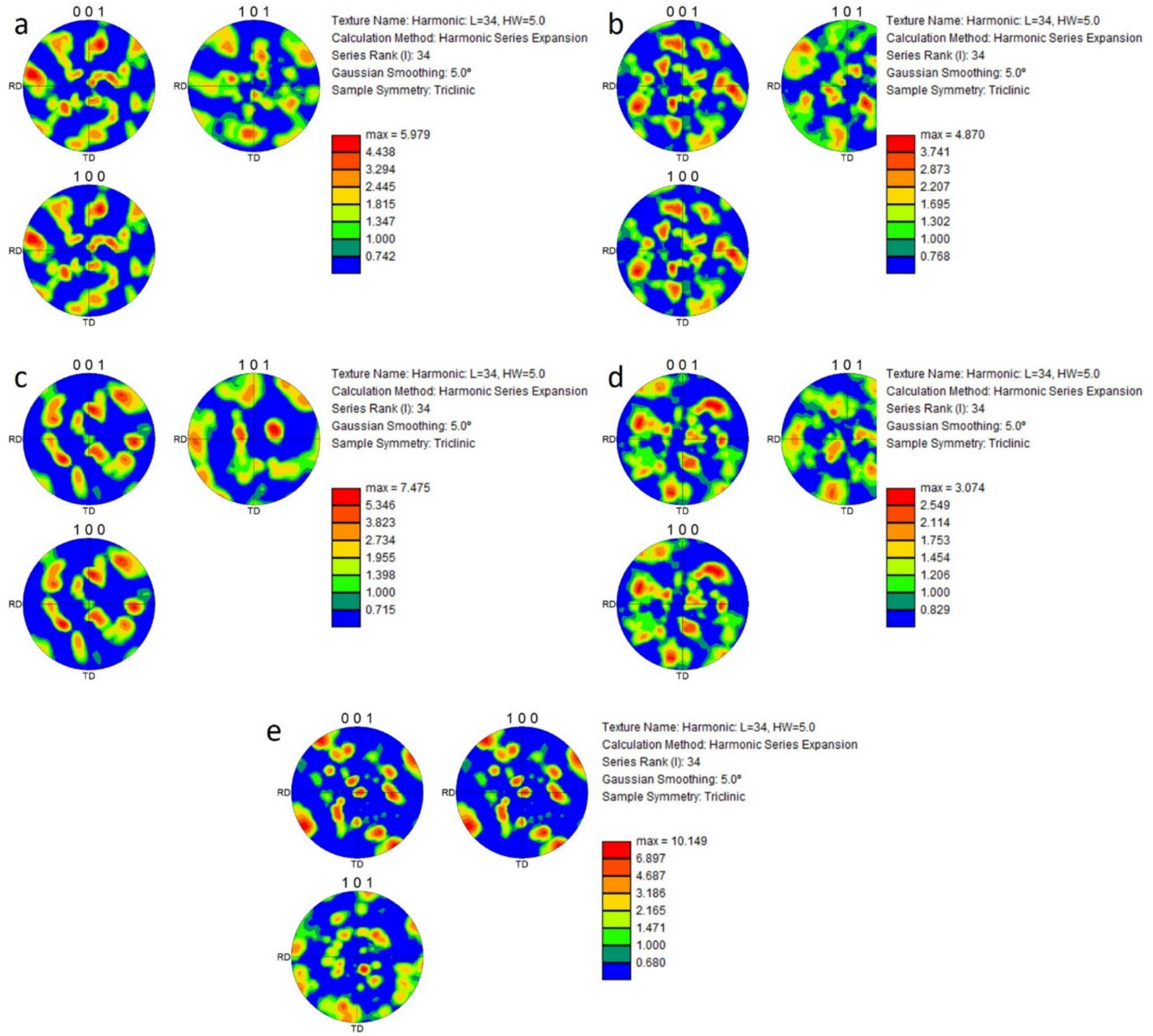

Fig. 10 Pole figures for sandwich desing taken from the locations; **a** hard-faced layer, **b** HAZ between base metal and hard-faced layer, **c** transition region between hard-faced layer and austenitic region, **d** HAZ between austenitic layer and base metal, and **e** austenitic layer. See for the locations in Fig. 8a

phases, which lead to localized changes in hardness, possibly also influenced by dilution effects.

In contrast, the sandwich joint (Fig. 12b) exhibits a more intricate hardness profile, with significant differences observed between the layers. The hardness values in this configuration are 199 ± 11 HV in the fifth (face) pass, similar to the austenitic joint, but then there is a substantial increase to 478 ± 48 HV in the fourth pass (the hard-faced layer), 212 ± 11 HV in the third, 207 ± 12 HV in the second, and 204 ± 6 HV in the first (root) pass. The results indicate a more pronounced variation in hardness from the face pass to the root pass. The marked increase in hardness within the hard-faced layer is attributed to the presence of martensitic phases and chromium carbides (Fig. 13). Additionally, both configurations show high hardness values in the HAZ regions of the final passes, particularly in the coarse-grained heat-affected zone (CGHAZ) and fine-grained heat-affected zone (FGHAZ), where the rapid cooling rates result in hardness levels exceeding 450 HV. However, in the HAZ of the lower layers, this hardness is reduced due to the tempering effect of subsequent welding passes, especially in the earlier layers.

On the other hand, a significant softening trend is evident in both welds, starting in the sub-critical heat-affected

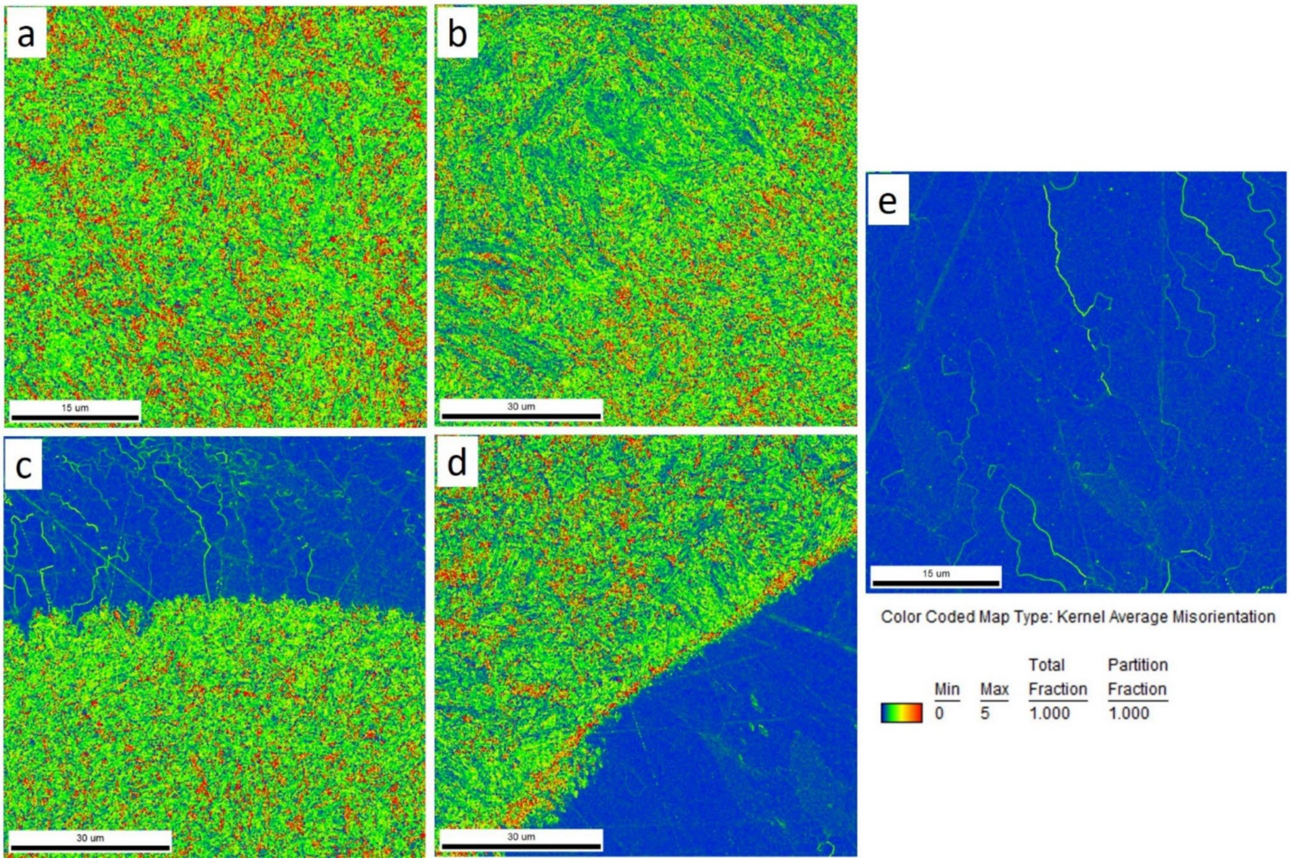

Fig. 11 Kemel average misorientation maps for sandwich desing taken from the locations; **a** hard-faced layer, **b** HAZ between base metal and hard-faced layer, **c** transition region between hard-faced layer and austenitic region, **d** HAZ between austenitic layer and base metal, and **e** austenitic layer. Se efor the locations in Fig. 8a

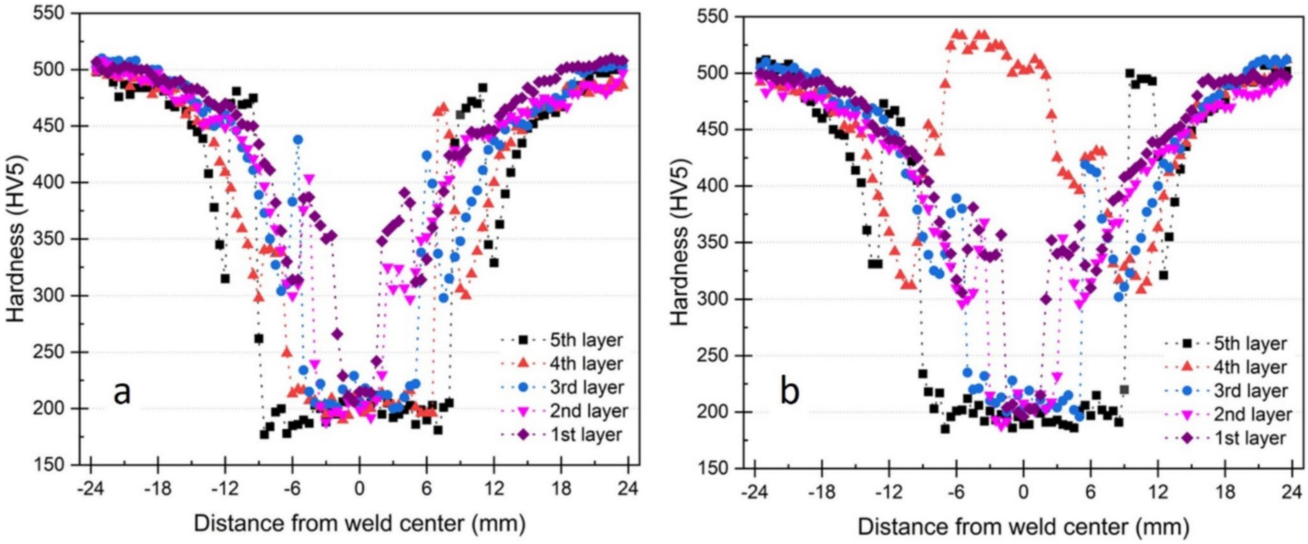

Fig. 12 Hardness test results for each layer; **a** austenitic and **b** sandwich joint

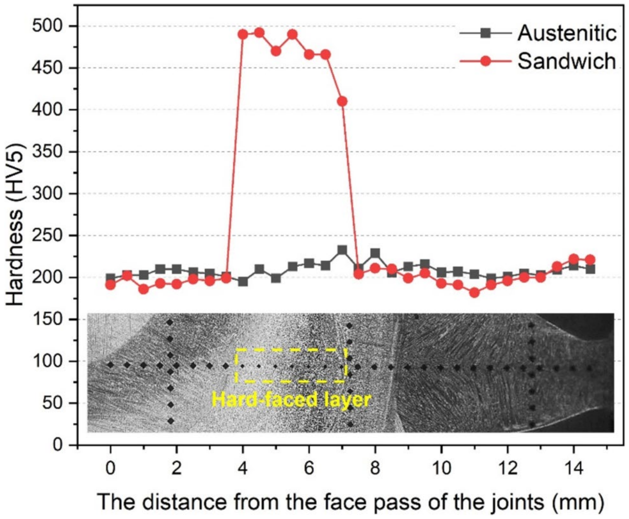

Fig. 13 Hardness variation from the face pass to the root pass across the layers

zone (SCHAZ) and extending into the intercritical heat-affected zone (ICHAZ), where the lowest hardness values are observed. Similar findings were also reported in previous studies [22] This marked reduction in hardness within these softened regions could potentially create a vulnerability, particularly under high-impact conditions, stress, or ballistic testing. A detailed comparison of the HAZ regions on the right side of each weld in Fig. 14 reveals that the hardness values in the sandwich weld are slightly higher than those in the austenitic weld across all zones (CGHAZ, FGHAZ, ICHAZ, and SCHAZ). However, this difference may vary depending on the specific location of measurement due to its minor difference. Overall, both configurations display a similar hardness pattern. It is also important to note that according to military standards MIL-A-46100 and MIL-STD-1185, a minimum hardness of 477 HB (equivalent to 509 HV) must be achieved within 15.9 mm from the weld toe on ballistic surfaces. In our study, the base metal hardness is reached at approximately 12–13 mm from the weld toe in both welds, demonstrating the effectiveness of the chosen robotic welding parameters and confirming their compliance with the stringent requirements for ballistic applications. Cabrilo et al. [34] also reported that by maintaining ideal preheating and inter-pass temperatures during Gas Metal Arc Welding (GMAW) of high-hardness armor steel, the welded joint's hardness can be sustained above 509 HB within a 15.9 mm from the weld metal axis, thereby adhering to military standards for ballistic protection.

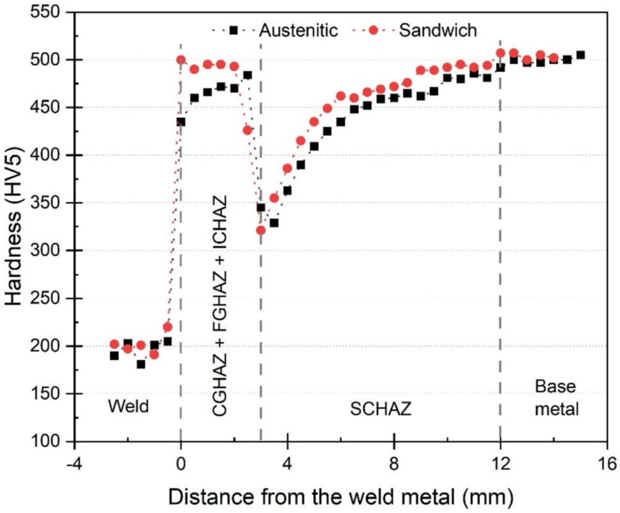

Fig. 14 Hardness test results showing the variation along the weld metal and HAZ regions

Figure 15 illustrates the chemical composition changes from the face pass to the root pass in the sandwich joint, which directly correlates with the observed increases in hardness. Notably, the chromium (Cr) content in the hard-faced layer rises to approximately 10%, exceeding the 8.53% Cr found in the hardfacing wire shown in Table 1. This increase is due to Cr diffusion from the austenitic wire, which contains 17.82% Cr. This enrichment in Cr plays a crucial role in the hardness increase observed in this area. Conversely, the nickel (Ni) content decreases as expected when transitioning from the austenitic wire, which contains 7.92% Ni, to the hardfacing wire, which contains just 0.18% Ni. This decrease is also consistent with the formation of brittle martensitic phases. Additionally, there is an increase in manganese (Mn) and iron (Fe) content, which reflects the mixing of filler materials.

Figure 16 exhibits the stress–strain curves for the base metal, austenitic, and sandwich joint designs, with the corresponding numerical data summarized in Table 4. These curves and data are crucial for analyzing the mechanical

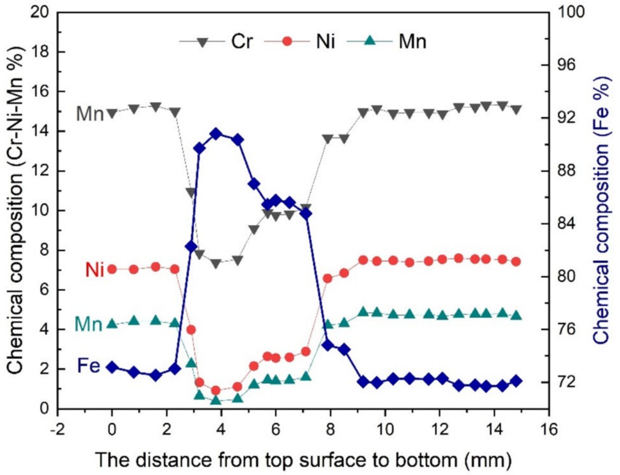

Fig. 15 Chemical composition variations from face pass to root pass

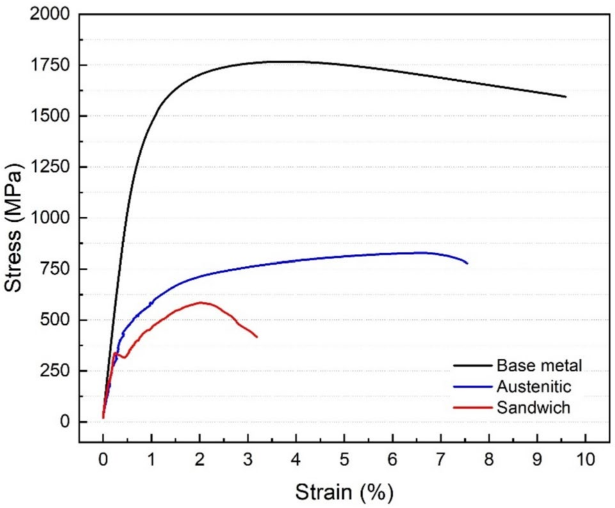

Fig. 16 Stress and strain curves for base metal, austenitic, and sandwich design

Table 4 Summary of tensile test results

	Yield Strength, MPa	Tensile strength, MPa	Elongation, % (lo:30 mm)
Base metal	1278 ± 35	1746 ± 42	9 ± 0.5
Austenitic	497 ± 4	808 ± 28	7.1 ± 0.2
Sandwich	295 ± 40	592 ± 11	2.7 ± 0.5

behavior of each material under tensile loading and for comparing the performance across different joint configurations. The base metal demonstrates the highest yield strength (1278 MPa) and tensile strength (1746 MPa), as well as the greatest elongation (9%), indicative of its hardened and tempered microstructure, which is optimized for ballistic protection. When comparing the austenitic joint to the base metal, there is a significant decrease in both yield strength and tensile strength, with yield strength reduced by approximately 61% and tensile strength by about 54%. Despite these reductions, the austenitic joint maintains a relatively higher strain capacity (7.1% elongation), only 21% lower than the base metal, highlighting its ductile nature. This ductility allows the austenitic joint to absorb more energy, thus preventing sudden failure under dynamic loading conditions. Nevertheless, it is essential to note that directly comparing elongation values with the base metal is not entirely accurate. Due to the uneven distribution of the low-yield-strength ER307 filler material within the V-groove weld, the gauge length (l0) includes portions of the base metal, which possesses a much higher yield strength of 1278 MPa. Consequently, the elongation value is reduced, as the base metal does not yield even at the fracture point. Reducing the gauge length (l0) would provide a more precise representation of the elongation specific to the both joints. This effect is clearly demonstrated in Fig. 17a, where necking is concentrated in the austenitic region, emphasizing the actual deformation. In contrast, the sandwich joint exhibits the lowest mechanical

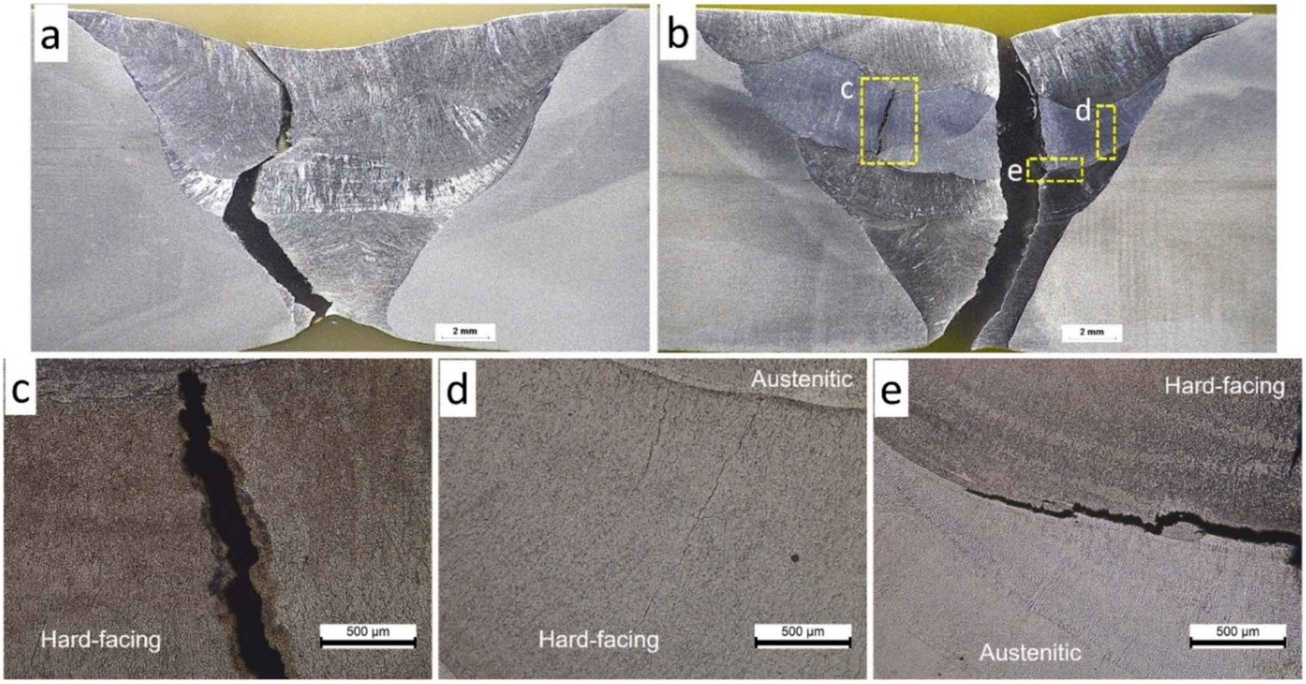

Fig. 17 Section view of tensile test specimens showing the breakage; **a** austenitic and **b**, **c**, **d**, **e** sandwich joint

properties among the three materials. Its yield strength and tensile strength decreased by 77%, 66%, and 70%, respectively, compared to the base metal. Compared to the austenitic joint, the sandwich design has 41% lower yield strength, 27% lower tensile strength, and 62% lower elongation. These reductions are primarily due to the hard-faced layer, which, while improving hardness, also introduces brittleness. This brittleness significantly limits the sandwich joint's ability to deform plastically under tensile stress, making it more susceptible to sudden failure.

Figure 17 presents sectional views of tensile test specimens, illustrating the fracture points for the austenitic (Fig. 17a) and sandwich (Fig. 17b–e) joints. These images are key to understanding the failure mechanisms in the different joint designs. The austenitic joint, shown in Fig. 17a, undergoes a ductile fracture characterized by significant necking and elongation prior to failure. This type of fracture is typical of materials with high toughness and ductility, capable of absorbing considerable energy before breaking. The presence of δ-ferrite and γ-austenite phases in the weld metal contributes to this ductile behavior, making the austenitic joint particularly suitable for applications where impact resistance and energy absorption are critical. On the other hand, the sandwich joint, depicted in Fig. 17b–e, shows a more complex failure pattern. The pronounced reduction in tensile properties observed in the sandwich joint can be attributed to the hard-faced layer. This layer is susceptible to stress and strain-induced micro-cracks, which form early during tensile loading. These micro-cracks reduce the effective cross-sectional area, leading to irregularities in the yield strength behavior. The sandwich joint exhibits evidence of brittle fracture in the hard-faced layer, likely due to its high hardness and reduced ductility resulting from the presence of martensitic phases and chromium carbides. This type of brittle fracture is less desirable in dynamic loading conditions, as it can lead to sudden and catastrophic failure. However, the sandwich joint also shows signs of ductile fracture in the underlying austenitic layer, indicating that the design retains

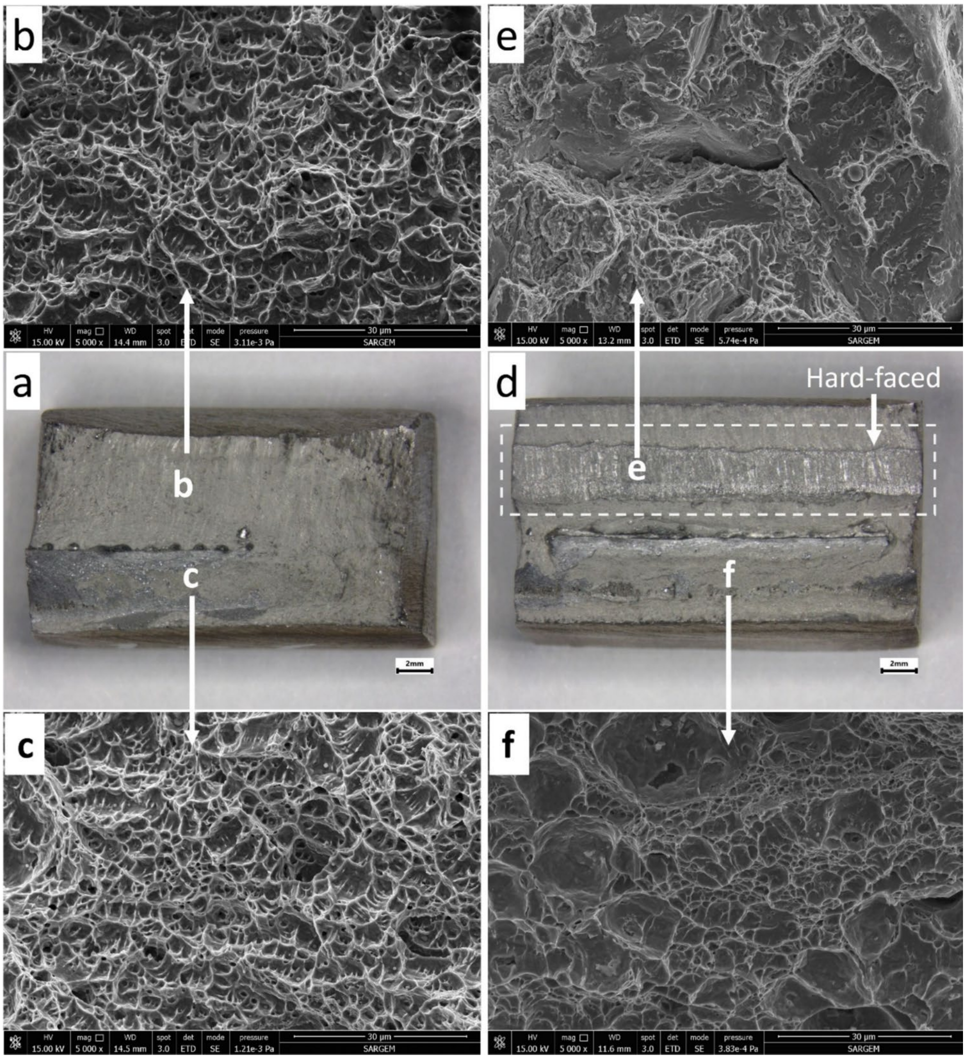

Fig. 18 Fracture surfaces of the tensile test specimens for; **a**–**c** austenitic and **d**–**f** sandwich joint

some degree of toughness, though still less than that of the fully austenitic joint.

Figure 18 illustrates the post-tensile test fracture surfaces of the austenitic and sandwich joints. Images (a) and (d) provide macroscopic views of the fracture surfaces for the austenitic and sandwich joints, respectively. The SEM images (b), (c), (e), and (f) correspond to specific regions labeled within images (a) and (d). The austenitic joint, as shown in Fig. 18a, exhibits a relatively uniform and ductile fracture surface. The SEM images in Fig. 18b and c reveal a highly ductile fracture mechanism, characterized by well-developed and uniformly distributed dimples which are typical indicators of ductile failure. The presence of equiaxed dimples indicates that void nucleation and coalescence dominated the fracture mechanism. These dimples also suggest significant plastic deformation occurred before the fracture, allowing the material to absorb a considerable amount of energy. This behavior aligns with the higher elongation and tensile strength observed during the tensile tests for the austenitic joint, where the ductile nature of the austenitic phase provided excellent resistance to fracture under tensile loading.

In contrast, the sandwich joint, depicted in Fig. 18d, displays a more complex fracture surface. The macroscopic view indicates a less uniform fracture compared to the austenitic joint. The SEM images in Fig. 18e and f reveal a mixed-mode fracture, with regions exhibiting both ductile and brittle characteristics. Figure 18e, corresponding to the hard-faced layer, reveals features characteristic of brittle fracture, including cleavage facets and intergranular cracks. These features suggest that the hard-faced layer, despite its high hardness, lacks sufficient ductility, leading to a brittle failure mode under tensile stress. This is similar to the micro-cracks observed in the section views of the tensile test specimens in Fig. 17. Furthermore, Fig. 18f, which corresponds to the underlying austenitic layer, shows also a combination of ductile dimples and brittle features. This mixed-mode fracture indicates the interaction between the tough austenitic layer and the brittle hard-faced layer. The presence of stress concentrations and micro-cracks in the hard-faced layer, which form early during tensile loading, likely contributes to the initiation of fracture in this region. These micro-cracks then propagate into the softer austenitic layer, resulting in the observed fracture pattern.

Figure 19 illustrates the Charpy-impact test results for the weld and HAZ regions, which are critical for evaluating the toughness of different joint designs, particularly under low-temperature conditions. Both designs comfortably meet and exceed the minimum toughness criteria set by the MIL-A-46100 standard (16.27 J for transverse and 18.98 J for longitudinal directions). In the austenitic joint, the weld region absorbs 66 J, while the HAZ region absorbs 101 J. Compared to the base metal, which has an impact energy of 20 J, the weld region shows more than a three times increase in toughness, and the HAZ exhibits an impressive five times increase. This significant enhancement in toughness is largely due to the austenitic phase, which is known for its capacity to absorb large amounts of energy without fracturing. This makes the austenitic joint particularly well-suited for applications subjected to sudden impacts or explosive forces.

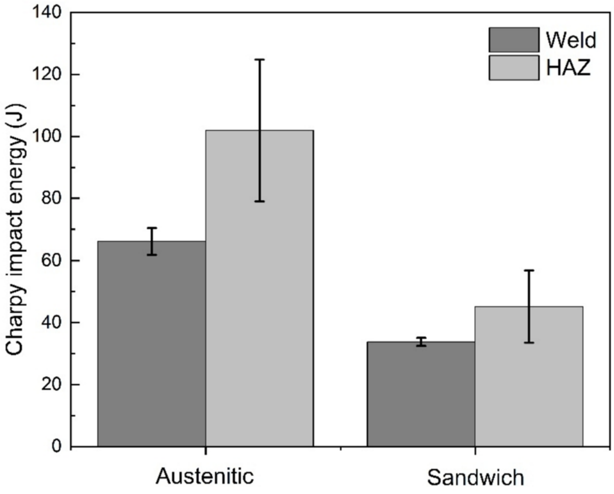

Fig. 19 Charpy-impact test results for weld and HAZ regions

In the case of the sandwich joint, the weld region absorbs 34 J, and the HAZ region absorbs 45 J. Although these values are lower than those recorded for the austenitic joint, they still represent a considerable improvement over the base metal. Specifically, the weld region of the sandwich joint is 70% tougher than the base metal, while the HAZ region shows a 125% increase in toughness relative to the base metal. However, the toughness of the sandwich joint's weld region is approximately 48% lower than that of the austenitic weld, and its HAZ region is 55% lower. The reduced toughness observed in the sandwich joint is primarily attributed to the hard-faced layer, which, although it enhances hardness, also introduces brittleness, making the joint more prone to brittle fracture under impact loading. In addition, the higher toughness values found in the HAZ regions of both joint designs, compared to their respective weld regions, can be attributed to the softening effect mentioned earlier. In these zones, the reduction in hardness increases the material's ability to absorb energy, resulting in the improved impact resistance observed in the HAZ due to the presence of tempered martensite.

Figure 20 presents the fracture surfaces of Charpy impact test specimens for both austenitic (a–c) and sandwich joint designs (d–f). The images include both macroscopic views (a, d) and fractographic examinations through SEM (b, c, e, f) to demonstrate the fracture mechanisms in each case. The austenitic joint exhibits a dense distribution of deep dimples

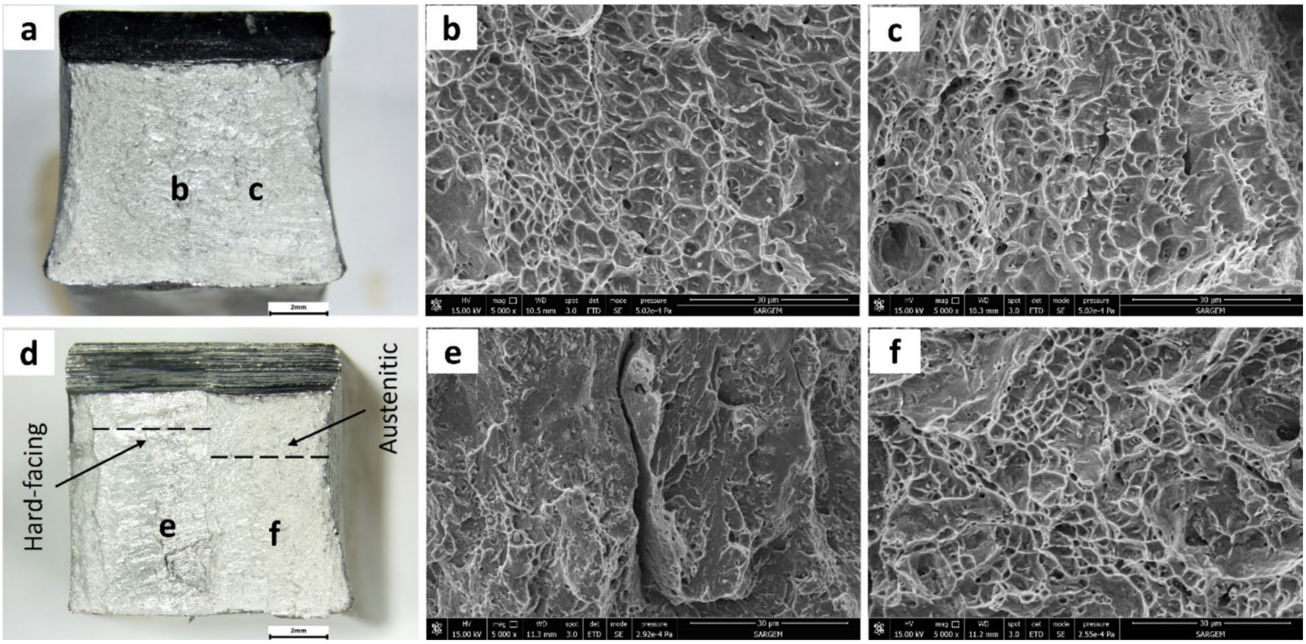

Fig. 20 Fracture surfaces of the Charpy impact test specimens for; **a**–**c** austenitic and **d**–**f** sandwich joint

and significant lateral expansion (0.80 mm), indicating a fully ductile fracture mechanism. The high energy absorption is attributed to extensive plastic deformation, enhancing the joint's toughness. In contrast, the sandwich joint design presents a mixed fracture mechanism, characterized by brittle failure in the hard-facing region (e) and ductile behavior in the austenitic region (f). The hard-faced area (e) predominantly displays quasi-cleavage and intergranular fracture features, with scarce dimples and a fracture morphology dominated by cleavage-like, flat, faceted regions. This suggests limited plastic deformation and increased susceptibility to brittle failure. In comparison, the austenitic region (f) in the sandwich joint exhibits a more pronounced dimpled structure, though the dimples are shallower and less uniformly distributed than those in the fully austenitic weld (b, c), indicating a reduction in ductility. Additionally, the lateral expansion of the sandwich joint (0.40 mm) is significantly lower than that of the austenitic weld, confirming that the incorporation of a hard-facing filler metal reduces the joint's overall toughness. These findings are consistent with Fig. 19, which shows that the austenitic weld joint absorbs considerably higher impact energy than the sandwich joint design.

For each joint design, one shot was conducted in each region—base metal, HAZ, and weld area—under the stringent conditions outlined by the EN 1522 FB7 standard. This standard is renowned for its rigorous requirements, making it an excellent benchmark for assessing the ballistic performance of armor steels. The bullet velocity for each shot was summarized in Table 5. The ballistic tests performed on the base metal slightly exceeded the range specified as 820 ± 10 m/s in the EN 1522 FB7, whereas the weld region and HAZ, which constitute the primary focus of this study, remained within the standard's defined limits.

Table 5 Bullet velocities used for each location of the joints and penetration evaluations (CP, complete penetration; PP, partial penetration)

Joint type	Weld region (m/s)	HAZ (m/s)	Base metal (m/s)
Austenitic	824.8 (CP)	829.9 (PP)	834.1 (PP)
Sandwich	816.7 (PP)	822.6 (PP)	836.6 (PP)

Figure 21 shows the ballistic test results for the austenitic design. The results reveal that the projectile fully penetrated the weld area, creating a significant exit hole. This outcome indicates that, although the austenitic weld offers some degree of resistance, it may not be adequate to prevent penetration under high-impact conditions completely. The complete penetration (CP) suggests that the ductility of the austenitic weld, while advantageous in tensile testing, may not provide the necessary hardness to stop a high-velocity projectile effectively.

In contrast, Fig. 22 illustrates that the projectile did not completely penetrate the weld area in the sandwich joint. The damage depth inflicted by the projectile in the sandwich weld was measured to be approximately 11 mm, indicating that the inclusion of a hard-faced interlayer in the sandwich design significantly improved the joint's ballistic resistance. This hard-faced layer provided additional hardness, which contributed to absorbing and deflecting the energy of the

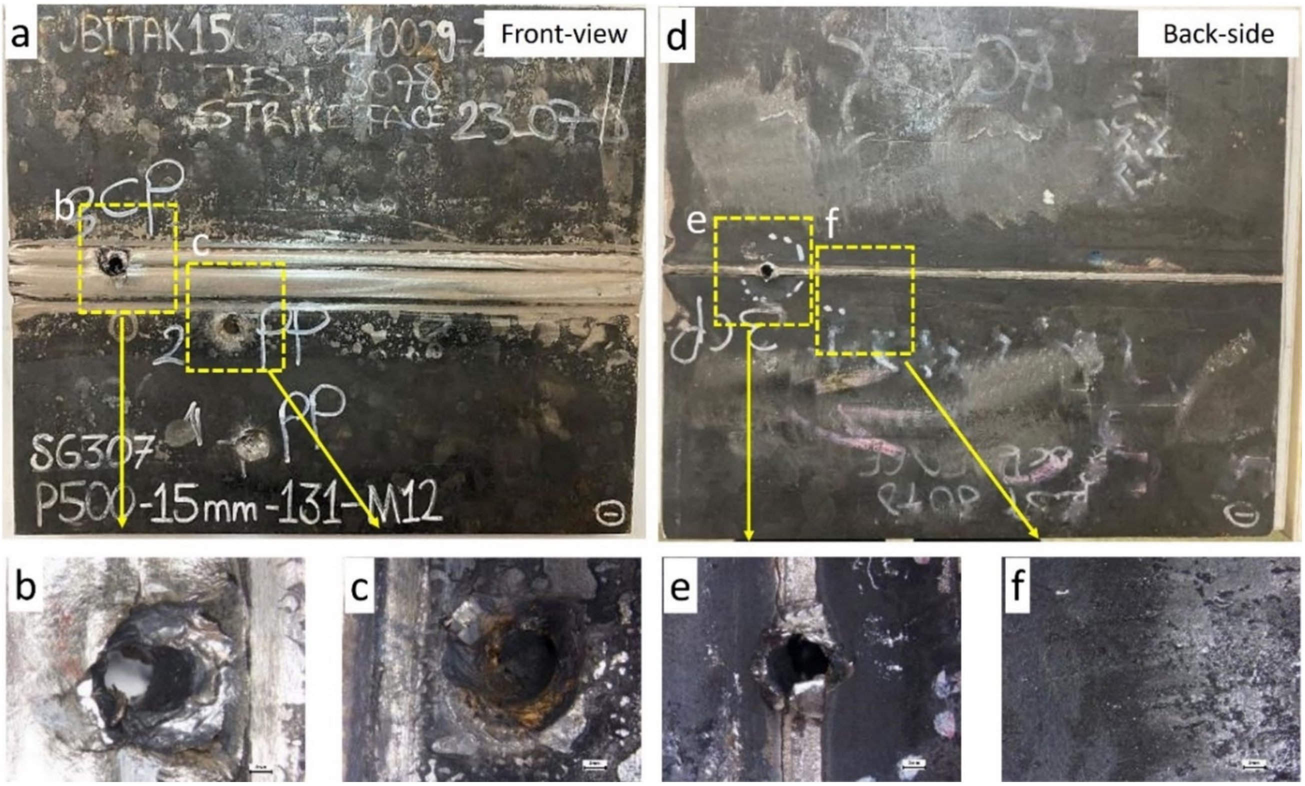

Fig. 21 Ballistic test results for austenitic design

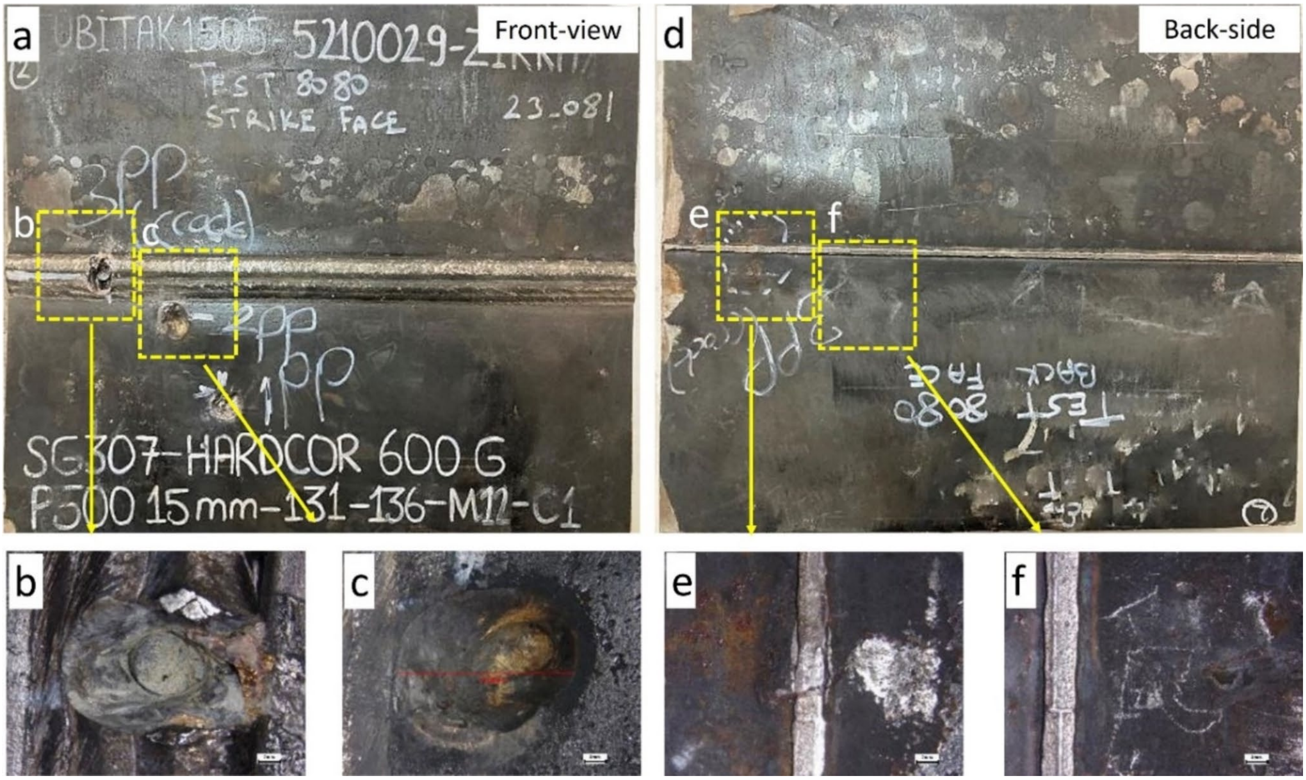

Fig. 22 Ballistic test results for sandwich design

incoming projectile, thereby preventing complete penetration. This outcome demonstrates the superiority of the sandwich design in enhancing ballistic performance compared to the fully austenitic design.

Figure 23 presents sectional views of the ballistic test results for the sandwich joint, with a focus on the base metal and HAZ regions. The cross-sectional analysis indicates that the base metal performed as anticipated, showing minimal deformation and effectively absorbing the energy from the ballistic impact. This performance aligns with the inherent properties of armor steel, which is engineered to provide high levels of ballistic resistance. On the other hand, the results in the HAZ are particularly noteworthy. Due to the relatively narrow softening zone within the HAZ, this region exhibited excellent resistance to penetration, with a measured penetration depth of only 6.8 mm This shallow penetration depth suggests that the HAZ retained its structural integrity under ballistic conditions. Additionally, as seen in Figs. 21 and 22, there was no observable bulging on the rear side of the HAZ region, underscoring the effectiveness of the weld design in preventing significant deformation or failure in this critical area.

Figure 24 provides a comparative analysis of the sectional views from ballistic tests conducted on the weld regions of both austenitic and sandwich designs. In the austenitic joint (Fig. 24a), the section reveals complete penetration through the weld, which aligns with previous observations that, although the austenitic weld is ductile, it lacks sufficient hardness to resist direct ballistic impact. In contrast, the sandwich joint (Fig. 24b) shows only partial penetration (PP), with the hard-faced layer effectively absorbing and dispersing the impact energy. These results reinforce the conclusion that the sandwich design, which combines hard-faced and austenitic layers, offers enhanced protection against ballistic impacts compared to the fully austenitic design.

4 Conclusion

This study presents a detailed analysis of fully austenitic and sandwich joints in armor steel, focusing on their microstructural characteristics, mechanical properties, and ballistic performance. The key findings are as follows:

- The all NDT results revealed that both the fully austenitic and sandwich designs adhere to stringent quality standards, ensuring both surface and volumetric integrity.
- The fully austenitic joint exhibited a uniform microstructure comprising δ-ferrite and γ-austenite phases, whereas the sandwich joint displayed a more complex structure with additional martensitic phases in the hard-faced layer.
- The hard-faced layer in the sandwich joint reached up to 478 HV, while the fully austenitic joint maintained consistent hardness values ranging from 196 to 225 HV. The optimized heat input values resulted in a precisely controlled HAZ width of 12–13 mm, effectively meeting the military standard limit of 15.9 mm.
- The sandwich joint demonstrated a significant reduction in impact toughness—55% in the HAZ (45 J) and 48% in the weld region (34 J) compared to the austenitic joint—yet still exceeded international standards. Despite this reduction, the HAZ regions in both joints absorbed considerably more energy—125% higher than the base metal

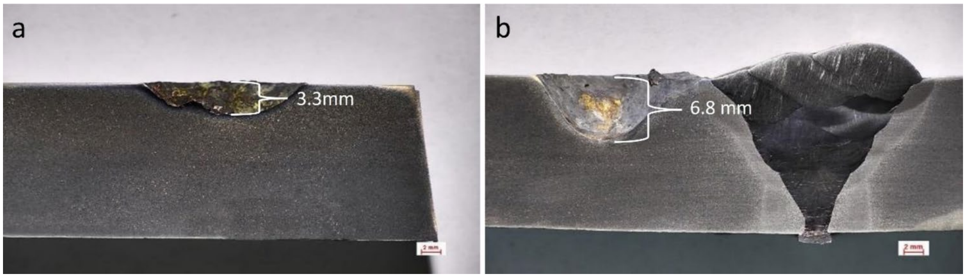

Fig. 23 Section view of ballistic test results for sandwich joint; **a** base metal and **b** HAZ

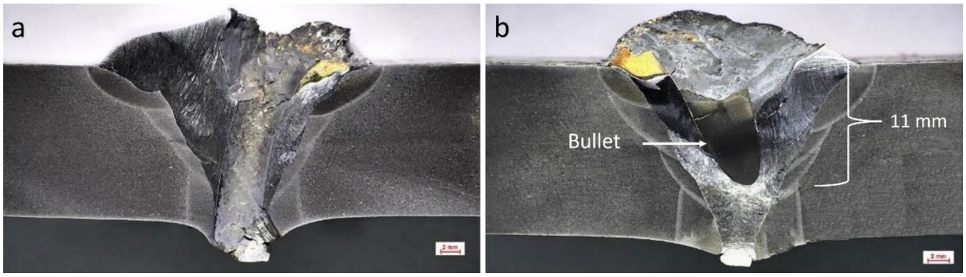

Fig. 24 Section view of ballistic test results for weld regions; **a** austenitic and **b** sandwich design

in the sandwich joint—due to the presence of tempered martensite.
- The tensile strengths of the austenitic and sandwich joints were 63% and 34% of the base metal, respectively. The sandwich joint showed decreased yield strength (41%), tensile strength (27%), and elongation (62%) compared to the austenitic joint.
- The sandwich joint offered superior ballistic resistance, with the hard-faced layer preventing complete penetration and limiting damage to 11 mm, whereas the austenitic joint could not stop the projectile and resulted in complete penetration. However, both designs showed partial deformation in the HAZ, successfully stopping the projectile.

In conclusion, the sandwich joint design significantly improves ballistic resistance due to its higher hardness, though this comes at the expense of reduced ductility and impact toughness. The results suggest that the developed welding design could lead to the establishment of new welding procedure specifications (WPS) and welding procedure qualification records (WPQR) to enhance the performance of welded armor steel joints in critical applications.

Acknowledgements The authors gratefully acknowledge Miilux OY Steel Company for providing the steel plates and Mr. Mert Basmacı's assistance in preparing them for welding. They also wish to acknowledge Mr. Batuhan Turgut's valuable contributions to conducting robotic welding operations.

Author contribution All authors read and approved the final manuscript. Ceren Çelik: material preparation, data collection, investigation, visualization, writing—original draft preparation. Uğur Gürol: conceptualization, investigation, methodology, validation, writing—original draft, review and editing, supervision.

Funding Open access funding provided by the Scientific and Technological Research Council of Türkiye (TÜBİTAK). This work was supported by the Scientific and Technological Research Council of Turkey (TÜBİTAK) under project number 5210029.

Data availability Data sets generated during the current study are available from the corresponding author on reasonable request.

Declarations

Competing ınterests The authors declare no competing interests.

Open Access This article is licensed under a Creative Commons Attribution 4.0 International License, which permits use, sharing, adaptation, distribution and reproduction in any medium or format, as long as you give appropriate credit to the original author(s) and the source, provide a link to the Creative Commons licence, and indicate if changes were made. The images or other third party material in this article are included in the article's Creative Commons licence, unless indicated otherwise in a credit line to the material. If material is not included in the article's Creative Commons licence and your intended use is not permitted by statutory regulation or exceeds the permitted use, you will need to obtain permission directly from the copyright holder. To view a copy of this licence, visit http://creativecommons.org/licenses/by/4.0/.

References

1. Robledo DM, Gomez JAS, Barrada JEG (2011) Development of a welding procedure for MIL A 46100 armor steel joints using gas metal arc welding. Dyna (Medellin) 78:65–71
2. Morsy MA, Abdel Aziz SM, Abdelwahed K, Abdelwahab SA (2022) Effect of welding parameters on the mechanical and metallurgical properties of armor steel weldment. J Eng Appl Sci 69. https://doi.org/10.1186/s44147-022-00102-7
3. Magudeeswaran G, Balasubramanian V, Madhusudan Reddy G (2018) Metallurgical characteristics of armour steel welded joints used for combat vehicle construction. Defence Technology 14:590–606. https://doi.org/10.1016/j.dt.2018.07.021
4. Vimal Kumar N, Uthayakumar M, Thirumalai Kumaran S, Velayudham A (2022) The effect of weld-groove surface modification on the joint performance of military grade armour steel: a sustainability approach. Mater Chem Phys 281. https://doi.org/10.1016/j.matchemphys.2022.125902
5. Magudeeswaran G, Balasubramanian V, Madhusudhan Reddy G (2008) Hydrogen induced cold cracking studies on armour grade high strength, quenched and tempered steel weldments. Int J Hydrogen Energy 33:1897–1908. https://doi.org/10.1016/j.ijhydene.2008.01.035
6. Gürol U, Karahan T, Erdöl S et al (2022) Characterization of armour steel welds using austenitic and ferritic filler metals. Trans Indian Inst Met 75:757–770. https://doi.org/10.1007/s12666-021-02464-7
7. Balaguru V, Balasubramanian V, Sivakumar P (2020) Effect of weld metal composition on impact toughness properties of shielded metal arc welded ultra-high hard armor steel joints. J Mech Behav Mater 29:186–194. https://doi.org/10.1515/jmbm-2020-0019
8. Čabrilo A, Janjić N (2022) Weldıng of hıgh-hardness armor steel. Adv Eng Letters 1:148–155. https://doi.org/10.46793/adeletters.2022.1.4.5
9. Sathish Kumar K, Arivazhagan N (2024) An innovative pulsed current arc welding technology for armor steel: processes, microstructure, and mechanical properties. Mater Today Commun 38. https://doi.org/10.1016/j.mtcomm.2024.108237
10 Çelik C, Göçmen M, Çoban O et al (2023) Yüksek Mukavemetli Balistik Zırh Çeliklerinin Kaynaklanabilirliği. Uludağ Univ J Faculty Eng 28:1009–1028
11. Son HJ, Jeong YC, Seo BW, et al (2023) Weld quality analysis of high-hardness armored steel in pulsed gas metal arc welding. Metals (Basel) 13. https://doi.org/10.3390/met13020303
12. Kim JS, Yi HJ (2017) Characteristics of GMAW narrow gap welding on the armor steel of combat vehicles. Appl Sci (Switzerland) 7. https://doi.org/10.3390/app7070658
13. Kim CJ, Jeong YC, Son HJ, et al (2024) Revolutionizing hardness via nanoparticle flux in welding of high-hardness armor steel. Mater Des 242. https://doi.org/10.1016/j.matdes.2024.113001
14. (2005) SSAB armox welding recommendation. OxelOsund
15. Magudeeswaran G, Balasubramanian V, Madhusudhan Reddy G (2014) Effect of welding processes and consumables on fatigue crack growth behaviour of armour grade quenched and tempered steel joints. Defence Technology 10:47–59. https://doi.org/10.1016/j.dt.2014.01.005

16. Kumar SN, Balasubramanian V, Malarvizhi S et al (2022) Effect of welding consumables on shielded metal arc welded ultra high hard armour steel joints. J Mech Behav Mater 31:8–21. https://doi.org/10.1515/jmbm-2022-0002
17. Saxena A, Kumaraswamy A, Madhusudhan Reddy G, Madhu V (2018) Influence of welding consumables on tensile and impact properties of multi-pass SMAW Armox 500T steel joints vis-a-vis base metal. Defence Technology 14:188–195. https://doi.org/10.1016/j.dt.2018.01.005
18. Naveen Kumar S, Balasubramanian V, Malarvizhi S et al (2022) Effect of welding consumables on the ballistic performance of shielded metal arc welded dissimilar armor steel joints. J Mater Eng Perform 31:162–179. https://doi.org/10.1007/s11665-021-06219-9
19. Alipooramirabad H, Paradowska A, Ghomashchi R, Reid M (2017) Investigating the effects of welding process on residual stresses, microstructure and mechanical properties in HSLA steel welds. J Manuf Process 28:70–81. https://doi.org/10.1016/j.jmapro.2017.04.030
20. Hanhold B, Babu SS, Cola G (2013) Investigation of heat affected zone softening in armour steels: part 1 - phase transformation kinetics. Sci Technol Weld Joining 18:247–252. https://doi.org/10.1179/1362171812Y.0000000100
21. Savic B, Cabrilo A (2021) Effect of heat input on the ballistic performance of armor steel weldments. Materials 14. https://doi.org/10.3390/ma14133617
22. Çoban O, Kaymak F, Gürol U, Koçak M (2023) Characterization of fillet welded armor steel performed by robotic gas metal arc welding: effect of heat ınput on microstructure and microhardness. J Mater Eng Perform. https://doi.org/10.1007/s11665-023-09058-y
23. Choo S, Baek E, Sunghak L (1996) Ballistic impact behaviour of multilayered armor plates processed by hardfacing. Metall and Mater Trans A 27:3335–3340
24. Babu S, Balasubramanian V, Madhusudhan Reddy G, Balasubramanian TS (2010) Improving the ballistic immunity of armour steel weldments by plasma transferred arc (PTA) hardfacing. Mater Des 31:2664–2669. https://doi.org/10.1016/j.matdes.2009.11.060
25. Reddy GM, Mohandas T, Papukutty K (1999) Enhancement of ballistic capabilities of soft welds through hardfacing. Int J Impact Eng 22:775–791. https://doi.org/10.1016/S0734-743X(99)00020-2
26. Gürol U, Çelik C, Çoban O, et al (2025) Mechanical and ballistic performance of high-hardness armor steels welded with ASS-LHF sandwich joint design. Mater Today Commun 42. https://doi.org/10.1016/j.mtcomm.2024.111209
27. Balakrishnan M, Balasubramanian V, Reddy G (2013) Effect of hardfaced ınterlayer thickness and low hydrogen ferritic capping on ballistic performance of shielded metal arc welded armour steel joints. J Iron Steel Res Int 20:82–91
28. Balakrishnan M, Balasubramanian V, Madhusudhan Reddy G, Parameswaran P (2013) Effect of capping front layer materials on the penetration resistance of Q&T steel welded joints against 7.62-mm armor-piercing projectile. Metall Mater Trans A Phys Metall Mater Sci 44:4218–4229. https://doi.org/10.1007/s11661-013-1794-8
29. Maweja K, Stumpf W (2008) The design of advanced performance high strength low-carbon martensitic armour steels. Microstructural considerations. Mater Sci Eng, A 480:160–166. https://doi.org/10.1016/j.msea.2007.07.078
30. Balakrishnan M, Balasubramanian V, Madhusuhan Reddy G, Sivakumar K (2011) Effect of buttering and hardfacing on ballistic performance of shielded metal arc welded armour steel joints. Mater Des 32:469–479. https://doi.org/10.1016/j.matdes.2010.08.037
31. Kumar A, Pandey C (2022) Some studies on dissimilar welds joint P92 steel and Inconel 617 alloy for AUSC power plant application. Int J Pressure Vessels and Piping 198. https://doi.org/10.1016/j.ijpvp.2022.104678
32. Maurya AK, Pandey C, Chhibber R (2021) Dissimilar welding of duplex stainless steel with Ni alloys: a review. Int J Pressure Vessels and Piping 192
33. Mert T, Gürol U, Tümer M (2023) The effect of weaving and non-weaving multi-pass procedure on microstructure and mechanical properties in GMAW of S960QL. Int J Adv Manuf Technol 129:4731–4742. https://doi.org/10.1007/s00170-023-12441-7
34. Cabrilo A, Geric K, Jovanovic M, Vukic L (2018) Weldability and ımpact energy properties of high-hardness armor steel. J Mater Eng Perform 27:1281–1295

Publisher's Note Springer Nature remains neutral with regard to jurisdictional claims in published maps and institutional affiliations.